

# Studying the $\rho$ resonance parameters with staggered fermions

Ziwen Fu<sup>1,2,\*</sup> and Lingyun Wang<sup>3,†</sup>

<sup>1</sup>Key Laboratory for Radiation Physics and Technology of Education Ministry;  
Institute of Nuclear Science and Technology, Chengdu 610064, China

<sup>2</sup>Center for Theoretical Physics, College of Physical Science and Technology, Sichuan University, Chengdu 610064, China

<sup>3</sup>International Affair Department, Chengdu Jiaxiang Foreign Language School, Chengdu 610023, China

We deliver a lattice study of  $\rho$  resonance parameters with  $p$ -wave  $\pi\pi$  scattering phases, which are extracted by finite-size methods at one center-of-mass frame and four moving frames for six MILC lattice ensembles with pion masses ranging from 346 to 176 MeV. The effective range formula is applied to describe the scattering phases as a function of the energy covering the resonance region, this allows us to extract  $\rho$  resonance parameters and to investigate the quark-mass dependence. Lattice studies with three flavors of the Asqtad-improved staggered fermions enable us to use the moving-wall source technique on large lattice spatial dimensions ( $L = 64$ ) and small light  $u/d$  quarks. Numerical computations are carried out at two lattice spacings,  $a \approx 0.12$  and  $0.09$  fm.

PACS numbers: 12.38.Gc, 11.15.Ha

## I. INTRODUCTION

Resonances decay into elementary particles via strong interaction, which is experimentally studied by scattering approaches. The theoretical computation of the resonance parameters from QCD is difficult because of its nonperturbative property. At present, it is practical to apply lattice QCD to calculate the scattering observables. The  $\rho$  meson is the simplest resonance for such a lattice study. The principal decay channel of the  $\rho$  meson is to a pair of pions with a branching rate close to 100.0% [1], which can be precisely handled with lattice QCD. Nonetheless, the reliable calculations of  $\pi\pi$  correlators are expensive; hence, the hadronic coupling constants were used in early studies of the  $\rho$  resonance parameters [2–7].

With the great progress of numerical algorithms, aided by the tremendous advancement of computer power, the finite-size formula established by Lüscher in the center-of-mass frame (CMF) [8, 9] and the extensions to the moving frame (MF) [10] have been employed to extract  $\rho$  resonance parameters from  $p$ -wave  $I = 1$   $\pi\pi$  scattering phases. Such an exploratory study was conducted by the CP-PACS Collaboration with Wilson fermions [11]. After this pioneering work, the QCDSF Collaboration delivered results with clover fermions [12], the ETMC Collaboration reported results with maximally twisted mass fermions and explored the pion mass dependence [13], J. Frison *et al.* presented preliminary results with Wilson fermions and pion masses as low as 200 MeV [14], Lang *et al.* delivered results with clover-Wilson fermions using Laplacian Heaviside smearing operators [15], and the PACS-CS Collaboration investigated them with Wilson fermions using the efficient smearing techniques [16]. Pelissier and Alexandru presented results from asymmetrical lattices using nHYP-smearred clover fermions [17].

The Hadron Spectrum Collaboration (HSC) adopted the anisotropic lattice formulation of clover fermions [18] and recently further used the coupled channel [19] to study  $\rho$  resonance parameters. Good statistical precision was obtained from anisotropic Wilson clover by J. Bulava *et al.* [20], and Guo *et al.* presented their results with nHYP-smearred clover fermions [21]. The RQCD Collaboration recently computed  $\rho$  resonance parameters at a nearly physical pion mass using nonperturbatively improved Wilson fermions [22].

It is well known that the rectangular diagrams of  $I = 1$   $\pi\pi$  scattering are hard to calculate, and the stochastic source method, or its variants (the distillation method, etc.) are normally used to study the  $\rho$  resonance [11–22]. Although it is luxury, the moving wall source technique, which has been explored in the center-of-mass frame [23, 24], is believed to calculate the rectangular diagram of the two-particle scattering with high quality. Recently we further extended this method to a two-particle system with nonzero momenta to tentatively investigate the  $\kappa$ ,  $\sigma$ , and  $K^*(892)$  meson decays [25], along with a few studies of the meson-meson scattering [26]. In these works, we found that the moving-wall source can calculate both the four-point and three-point correlators with high quality; this encourages us to exploratively use this technique to study  $\rho$  resonance parameters.

The rapid deterioration of the pion propagator signal as momentum increases is impressive [27]. According to the analytical arguments in Ref. [28], the noise-to-signal ratio  $R_{NS}(t)$  of pion energy  $E_\pi(\mathbf{p} = \frac{2\pi}{L}\mathbf{n})$  grows exponentially as  $R_{NS}(t) \propto \frac{1}{\sqrt{N_c}} \exp(\sqrt{m_\pi^2 + \frac{4\pi^2}{L^2}\mathbf{n}^2} - m_\pi)t$ , where  $N_c$  is the number of gauge configurations. Consequently, for a given momentum  $\mathbf{p}$ , one of the most efficient ways to improve the statistics is to choose lattice ensembles with higher lattice spatial dimension  $L$  (see more discussion in the Appendix), which are explored by RQCD [22].

It is economical to perform lattice studies using staggered fermions compared to using other discretizations;

\* fuziwen@scu.edu.cn

† ylingyunwang@yahoo.com

this permits lattice examinations with the larger lattice spatial dimensions  $L$  or smaller quark masses within limited computer resources. For this reason, we first use staggered fermions to examine  $\rho$  resonance parameters, and then carry out lattice calculations on MILC lattice ensembles with Asqtad-improved staggered sea quarks (we use two ensembles with  $L = 40$  and one ensemble with  $L = 64$ ). This not only allows us to measure the pion energy for higher momenta with high quality, but also enables us to study  $\pi\pi$  scattering for the moving frame with total momentum  $\mathbf{P} = (2\pi/L)(\mathbf{e}_1 + \mathbf{e}_2 + \mathbf{e}_3)$  and  $\mathbf{P} = (2\pi/L)2\mathbf{e}_3$ , which are explored by HSC [18].

To map out the resonance region efficiently, for each lattice ensemble we study the  $I = 1$   $\pi\pi$  system with five Lorentz frames, one CMF and four MFs. The first moving frame is implemented with total momentum  $\mathbf{P} = (2\pi/L)\mathbf{e}_3$  (MF1), the second moving frame with  $\mathbf{P} = (2\pi/L)(\mathbf{e}_1 + \mathbf{e}_2)$  (MF2), and the third moving frame with  $\mathbf{P} = (2\pi/L)(\mathbf{e}_1 + \mathbf{e}_2 + \mathbf{e}_3)$  (MF3), where the  $\mathbf{e}_i$  is a unit vector in the spatial direction  $i$ . For the large lattice space (i.e.,  $L \geq 32$ ), we also use a fourth moving frame with  $\mathbf{P} = (2\pi/L)2\mathbf{e}_3$  (MF4). For a CMF, we extract the  $p$ -wave scattering phase only from the energy levels of the ground state; for each of the MFs, we extract them from the energy levels of the ground state and the first excited state: consequently, we can obtain the scattering phases at seven or nine energies for six MILC lattice ensembles. We will find that usually at least four energies are calculated for the  $p$ -wave  $I = 1$   $\pi\pi$  scattering phases, which either lie in or are in the vicinity of the resonance range  $[m_\rho - \Gamma_\rho, m_\rho + \Gamma_\rho]$ .

The lattice ensemble parameters of the MILC gauge configurations have been reliably determined by the MILC Collaboration [29, 30]. Our lattice simulation used six pion masses ranging from 346 to 176 MeV, ensuring that the physical kinematics for the  $\rho$ -meson decay,  $m_\pi/m_\rho < 0.5$ , is satisfied. Moreover, the computation of  $\rho$  resonance parameters at six lattice ensembles allows us, following the ETMC Collaboration [13], to investigate the pion mass dependence of the resonance mass and decay width and, hence, to reliably perform a chiral extrapolation to the physical point. Additionally, our numerical calculations of the  $\pi\pi$  correlators are for the first time calculated with the moving-wall source, which allows us to obtain results with high statistics. Moreover, according to the discussion in the Appendix, the usage of lattice ensembles with relatively large  $L$  and the summations of the  $\rho$  correlator over all the even time slices and the  $\pi\pi$  correlator over all the time slices also significantly improved the signals of the corresponding correlators.

This article is organized as follows. In Sec. II, we elaborate on our calculation method. Our concrete lattice calculations are provided in Sec. III. We deliver our lattice results in Sec. IV, provide analysis in Sec. V, and reach our conclusions and outlooks in Sec. VI. Discussions of the noise-to-signal ratio of correlator are left to the Appendix.

## II. FINITE-VOLUME METHODS

In the present study, we will examine the neutral  $\rho$ -meson decay into a pair of pions in the  $p$ -wave state, and concentrate on  $\pi\pi$  system with the isospin representation of  $(I, I_z) = (1, 0)$ . We restrict ourselves to the overall momenta  $\mathbf{P} = [0, 0, 0]$ ,  $[0, 0, 1]$ ,  $[1, 1, 0]$ ,  $[1, 1, 1]$  and  $[0, 0, 2]$ .<sup>1</sup>

### A. Center-of-mass frame

In the center-of-mass frame, the energy levels of two free pions are provided by

$$E = 2\sqrt{m_\pi^2 + |\mathbf{p}|^2},$$

where  $\mathbf{p} = \frac{2\pi}{L}\mathbf{n}$ , and  $\mathbf{n} \in \mathbb{Z}^3$ . For the lattice ensembles with enough large  $L$  and small pion masses, the lowest energy  $E$  for  $\mathbf{n} \neq 0$  [e.g.,  $\mathbf{n} = (1, 0, 0)$ ] is usually in the vicinity of the lattice-measured  $\rho$  mass  $m_\rho$ . Therefore, we will pay special attention to the  $\mathbf{n} = (1, 0, 0)$  case. In fact, we indeed calculate the energy levels for the  $\mathbf{n} = (1, 1, 0)$  and  $\mathbf{n} = (1, 1, 1)$  cases. Unfortunately, almost all of these energy levels either turned out to be beyond  $4\pi$  threshold or the relevant signals were not good enough. We should remark at this point that the finite-volume methods are only valid for the elastic scattering; consequently, we are only interested in the energy levels of the  $\pi\pi$  system in the elastic region  $2m_\pi < E < 4m_\pi$ .

In the presence of the interaction between two pions, the energy levels of the  $\pi\pi$  system are displaced by the hadronic interaction from  $E$  to  $\bar{E}$ ,

$$\bar{E} = 2\sqrt{m_\pi^2 + k^2}, \quad k = \frac{2\pi}{L}q,$$

where the dimensionless scattering momentum  $q \in \mathbb{R}$ . These energy levels transform as the irreducible representation  $T_1^-$  under the cubic group  $O_h$ . The Lüscher formula links the energy  $\bar{E}$  to the  $p$ -wave  $\pi\pi$  scattering phase  $\delta_1$  [8, 9],

$$\tan \delta_1(k) = \frac{\pi^{3/2}q}{\mathcal{Z}_{00}(1; q^2)}, \quad (1)$$

where the zeta function is formally defined by

$$\mathcal{Z}_{00}(s; q^2) = \frac{1}{\sqrt{4\pi}} \sum_{\mathbf{n} \in \mathbb{Z}^3} \frac{1}{(|\mathbf{n}|^2 - q^2)^s}. \quad (2)$$

The zeta function  $\mathcal{Z}_{00}(s; q^2)$  can be efficiently evaluated by the method described in Ref. [31]. We notice an equivalent Lüscher formula has been recently developed in Ref. [32].

<sup>1</sup> The momentum is written in units of  $\frac{2\pi}{L}$ . For easy notation, in some places of this paper, the square braces are adopted to suggest a suppression of the dimensional factor, to be specific,  $\mathbf{P} = [0, 0, 0]$  denotes a momentum of  $(0, 0, 0)\frac{2\pi}{L}$ .

## B. Moving frame

Using a moving frame with nonzero total momentum  $\mathbf{P} = (2\pi/L)\mathbf{d}$ ,  $\mathbf{d} \in \mathbb{Z}^3$ , the energy levels of two free pions are expressed by

$$E_{MF} = \sqrt{m_\pi^2 + |\mathbf{p}_1|^2} + \sqrt{m_\pi^2 + |\mathbf{p}_2|^2},$$

where  $\mathbf{p}_1$ ,  $\mathbf{p}_2$  denote the three-momenta of the pions, which obey the periodic boundary condition,  $\mathbf{p}_1 = \frac{2\pi}{L}\mathbf{n}_1$ ,  $\mathbf{p}_2 = \frac{2\pi}{L}\mathbf{n}_2$ ,  $\mathbf{n}_1, \mathbf{n}_2 \in \mathbb{Z}^3$ , and total momentum  $\mathbf{P}$  is  $\mathbf{P} = \mathbf{p}_1 + \mathbf{p}_2$  [10].

In the presence of an interaction between two pions, the energy  $E_{CM}$  is

$$E_{CM} = 2\sqrt{m_\pi^2 + p^{*2}}, \quad p^* = \frac{2\pi}{L}q, \quad (3)$$

where the dimensionless momentum  $q \in \mathbb{R}$ ,  $p^* = |\mathbf{p}^*|$ , and  $\mathbf{p}^*$  are quantized to the values  $\mathbf{p}^* = \frac{2\pi}{L}\mathbf{r}$ ,  $\mathbf{r} \in P_{\mathbf{d}}$ , and the set  $P_{\mathbf{d}}$  is

$$P_{\mathbf{d}} = \left\{ \mathbf{r} \mid \mathbf{r} = \bar{\gamma}^{-1} \left[ \mathbf{n} + \frac{\mathbf{d}}{2} \right], \mathbf{n} \in \mathbb{Z}^3 \right\}, \quad (4)$$

where  $\bar{\gamma}^{-1}$  is the inverse Lorentz transformation operating in the direction of the center-of-mass velocity  $\mathbf{v}$ ,  $\bar{\gamma}^{-1}\mathbf{p} = \gamma^{-1}\mathbf{p}_{\parallel} + \mathbf{p}_{\perp}$ , where  $\mathbf{p}_{\parallel}$  and  $\mathbf{p}_{\perp}$  are the ingredients of  $\mathbf{p}$  parallel and perpendicular to  $\mathbf{v}$ , respectively. Using the Lorentz transformation, the energy  $E_{CM}$  is connected to the  $E_{MF}$  through  $E_{CM}^2 = E_{MF}^2 - \mathbf{P}^2$ .

The scattering phase shifts are expressed in terms of the generalized zeta function

$$\mathcal{Z}_{\ell m}^{\mathbf{d}}(s; q^2) = \sum_{\mathbf{r} \in P_{\mathbf{d}}} \frac{r^\ell Y_{\ell m}(\Omega_{\mathbf{r}})}{(r^2 - q^2)^s}, \quad (5)$$

where the set  $P_{\mathbf{d}}$  is defined in Eq. (4), the  $Y_{\ell m}$  are the spherical harmonic functions, and  $\Omega_{\mathbf{r}}$  stands for the solid angle parameters  $(\theta, \phi)$  of  $\mathbf{r}$  in spherical coordinates.

The first moving frame (MF1) is taken with  $\mathbf{d} = \mathbf{e}_3$ , and the energy levels of the  $\pi\pi$  system transform under the tetragonal group  $D_{4h}$ . The irreducible representations  $A_2^-$  and  $E^-$  are associated with the  $p$ -wave  $\pi\pi$  scattering states in a torus. In this work, we are only interested in the  $A_2^-$  sector due to limited computer resources; the energy levels  $\bar{E}$  are linked to the  $p$ -wave  $\pi\pi$  scattering phase shift  $\delta_1$  with the Rummukainen-Gottlieb formula for the  $A_2^-$  representation [10],

$$\tan \delta_1(q) = \frac{\gamma\pi^{3/2}q}{\mathcal{Z}_{00}^{\mathbf{d}}(1; q^2) + \frac{2}{\sqrt{5}}q^{-2}\mathcal{Z}_{20}^{\mathbf{d}}(1; q^2)}, \quad (6)$$

where the higher scattering phase shifts  $\delta_\ell (\ell \geq 3)$  are ignored, and the dimensionless center-of-mass scattering momentum  $q$  is calculated from the lattice-measured energies of the  $\pi\pi$  system through Eq. (3). The boost factor  $\gamma$  is calculated by  $\gamma = E_{MF}/E_{CM}$ .

We implemented the second moving frame (MF2) with  $\mathbf{d} = \mathbf{e}_1 + \mathbf{e}_2$ , and the corresponding energy levels of

the  $\pi\pi$  system transform under the orthorhombic group  $D_{2h}$ . The irreducible representations  $A_1^-$ ,  $B_1^-$ , and  $B_2^-$  occur for  $p$ -wave  $\pi\pi$  scattering states in a torus. In this work, we concentrate on the  $B_1^-$  sector; the corresponding finite-size formula for  $B_1^-$  representation is given by [10, 13, 15, 33]

$$\tan \delta_1(k) = \frac{\gamma\pi^{3/2}q}{\mathcal{Z}_{00}^{\mathbf{d}}(1; q^2) - \frac{1}{\sqrt{5}}q^{-2}\mathcal{Z}_{20}^{\mathbf{d}}(1; q^2) - i\sqrt{\frac{6}{5}}q^{-2}\mathcal{Z}_{22}^{\mathbf{d}}(1; q^2)}, \quad (7)$$

where the higher scattering phase shifts  $\delta_\ell (\ell \geq 3)$  are ignored.

In order to acquire more eigenenergies in the resonance region, we considered the third moving frame (MF3) with  $\mathbf{d} = \mathbf{e}_1 + \mathbf{e}_2 + \mathbf{e}_3$ . The corresponding energy eigenstates transform under the orthorhombic group  $D_{3d}$ . The irreducible representations  $A_2^-$ , and  $E^-$  occur for the  $p$ -wave  $\pi\pi$  scattering states in a torus. Here we are only interested in the  $A_2^-$  sector; the corresponding finite-size formula for MF3 with  $A_2^-$  representation is provided by [18, 33]

$$\cot \delta_1(k) = \frac{1}{\gamma\pi^{3/2}q} \left\{ \mathcal{Z}_{00}^{\mathbf{d}}(1; q^2) - i\sqrt{\frac{8}{15}}\frac{1}{q^2}\mathcal{Z}_{22}^{\mathbf{d}}(1; q^2) - \sqrt{\frac{8}{15}}\frac{1}{q^2} [\text{Re}\mathcal{Z}_{21}^{\mathbf{d}}(1; q^2) + \text{Im}\mathcal{Z}_{21}^{\mathbf{d}}(1; q^2)] \right\}, \quad (8)$$

where we overlook the higher scattering phase shifts  $\delta_\ell (\ell \geq 3)$  as well.

For large lattice ensembles (i.e.,  $L \geq 32$ ), the fourth moving frame (MF4) with  $\mathbf{d} = 2\mathbf{e}_3$  is also considered, and the energy levels of  $\pi\pi$  system transform under the tetragonal group  $D_{4h}$ . The irreducible representations  $A_2^-$  and  $E^-$  are associated with the  $p$ -wave  $\pi\pi$  scattering states in a torus. We here concentrate on the  $A_2^-$  sector. The energy levels  $\bar{E}$  linked to the  $p$ -wave  $\pi\pi$  scattering phase shift  $\delta_1$  with the Rummukainen-Gottlieb formula for the  $A_2^-$  representation can be calculated by Eq. (6).

The calculation method of zeta functions  $\mathcal{Z}_{00}^{\mathbf{d}}(1; q^2)$ ,  $\mathcal{Z}_{21}^{\mathbf{d}}(1; q^2)$ , and  $\mathcal{Z}_{22}^{\mathbf{d}}(1; q^2)$  is elaborated in Appendix A of Ref. [31], where we also gave its extensions in the two-particle system with arbitrary masses [25]. In this work, we are particularly interested in a MF3, with one pion at rest and one pion with momentum  $\mathbf{p} = (2\pi/L)(\mathbf{e}_1 + \mathbf{e}_2 + \mathbf{e}_3)$ , and a MF4, with one pion at rest and one pion with momentum  $\mathbf{p} = (4\pi/L)\mathbf{e}_3$ . For our concrete calculations, we found that the relevant scattering phases are usually calculated at energies which are more efficiently used to directly mark out the resonance region.

In this work, we only calculate the scattering phase of the ground state for the  $\mathbf{T}_1^-$  representation, since the relevant eigenenergies are expected to be much smaller than those of the excited states [16]. For the  $\mathbf{A}_2^-$  and the  $\mathbf{B}_1^-$  representations, we will also calculate the scattering phase shift for the first excited state. The relevant representations for the ground and the first excited states with the isospin  $(I, I_z) = (1, 0)$  are summarized in Table I.

TABLE I. Summary of the irreducible representations for the ground and first excited states with the isospin  $(I, I_z) = (1, 0)$ , where  $\mathbf{P}$  denotes total momentum,  $g$  gives the rotational group in each frame and  $\Gamma$  shows the relevant irreducible representation. The two-pion operators  $\mathcal{O}_{\pi\pi}$  and rho operators  $\mathcal{O}_\rho$  are listed in Column 5 and 6, respectively. The vectors in parentheses behind  $\pi$  and  $\rho$  represent the momenta of the two-pion state and the  $\rho$  meson in units of  $2\pi/L$ , respectively.

Frame	$\mathbf{P}$	$g$	$\Gamma$	$\mathcal{O}_{\pi\pi}$	$\mathcal{O}_\rho$
CMF	[0, 0, 0]	$\mathcal{O}_h$	$T_1^-$	$\pi(0, 0, 1)\pi(0, 0, -1)$	$(\rho_1 + \rho_2 + \rho_3)(0, 0, 0)$
MF1	[0, 0, 1]	$D_{4h}$	$A_2^-$	$\pi(0, 0, 1)\pi(0, 0, 0)$	$\rho_3(0, 0, 1)$
MF2	[1, 1, 0]	$D_{2h}$	$B_1^-$	$\pi(1, 1, 0)\pi(0, 0, 0)$	$(\rho_1 + \rho_2)(1, 1, 0)$
MF3	[1, 1, 1]	$D_{3h}$	$A_2^-$	$\pi(1, 1, 1)\pi(0, 0, 0)$	$(\rho_1 + \rho_2 + \rho_3)(1, 1, 1)$
MF4	[0, 0, 2]	$D_{4h}$	$A_2^-$	$\pi(0, 0, 2)\pi(0, 0, 0)$	$\rho_3(0, 0, 2)$

### C. Variational analysis

In order to extract the energy eigenvalues of the lower two states for the  $\mathbf{A}_2^-$  and the  $\mathbf{B}_1^-$  representations discussed in Sec. II—i.e.,  $\bar{E}_n$  ( $n = 1, 2$ )—the state-of-the-art variational method [9] is exploited for Wilson fermions. Moreover, corrections to the true energy levels are discussed in detail when the energies are extracted from the generalized eigenvalues [34]. These methods can readily be applied to staggered fermions with a small alteration [35]. In practice, we employ a two-dimensional variational basis and build the correlation function matrix,

$$C(t) = \begin{pmatrix} \langle 0 | \mathcal{O}_{\pi\pi}^\dagger(\mathbf{p}, t) \mathcal{O}_{\pi\pi}(\mathbf{p}, 0) | 0 \rangle & \langle 0 | \mathcal{O}_{\pi\pi}^\dagger(\mathbf{p}, t) \mathcal{O}_\rho(\mathbf{p}, 0) | 0 \rangle \\ \langle 0 | \mathcal{O}_\rho^\dagger(\mathbf{p}, t) \mathcal{O}_{\pi\pi}(\mathbf{p}, 0) | 0 \rangle & \langle 0 | \mathcal{O}_\rho^\dagger(\mathbf{p}, t) \mathcal{O}_\rho(\mathbf{p}, 0) | 0 \rangle \end{pmatrix}, \quad (9)$$

where  $\mathcal{O}_\rho$  is an interpolator for the neutral  $\rho$  meson with the specified momentum  $\mathbf{p}$  and the polarization vector parallel to the  $\rho$  momentum  $\mathbf{p}$ , and  $\mathcal{O}_{\pi\pi}$  is an interpolator for the  $\pi\pi$  system with the given total momentum  $\mathbf{P} = \mathbf{p}$ .

#### 1. $\pi\pi$ sector

In this section, the original definitions and notations are employed to review the basic formula for the lattice calculation of the  $p$ -wave scattering phase of the  $I = 1$   $\pi\pi$  system enclosed in a cubic torus [23, 24]. Let us concentrate on the scattering of two Nambu-Goldstone pions in the Kogut-Susskind staggered fermion formalism.

We build the  $\pi\pi$  interpolator with the isospin representation  $(I, I_z) = (1, 0)$  as [11, 14]

$$\mathcal{O}_{\pi\pi}^{I=1}(\mathbf{p}, \mathbf{q}; t) = \frac{1}{\sqrt{2}} (\pi^+(\mathbf{q}, t) \pi^-(\mathbf{p}, t+1) - \pi^+(\mathbf{p}, t) \pi^-(\mathbf{q}, t+1)), \quad (10)$$

where the pion momenta  $\mathbf{p} \neq \mathbf{q}$  and the total momentum of the  $\pi\pi$  system  $\mathbf{P} = \mathbf{p} + \mathbf{q}$ . In order to avoid the complicated Fierz rearrangement of quark lines [24], we choose creation operators at time slices that are different by one lattice time spacing.

The operator that creates a single pion with nonzero momentum  $\mathbf{p}$  from the vacuum is obtained by the Fourier transform  $\mathcal{O}_\pi(\mathbf{p}, t) = \sum_{\mathbf{x}} e^{i\mathbf{p}\cdot\mathbf{x}} \mathcal{O}_\pi(\mathbf{x}, t)$ , where the pion interpolators are denoted by  $\mathcal{O}_{\pi^+}(\mathbf{x}, t) = -\bar{d}(\mathbf{x}, t) \gamma_5 u(\mathbf{x}, t)$ ,  $\mathcal{O}_{\pi^-}(\mathbf{x}, t) = \bar{u}(\mathbf{x}, t) \gamma_5 d(\mathbf{x}, t)$ .

In the present work, we will concentrate on the five irreducible representations,  $T_1^-$ ,  $A_2^-$ ,  $B_1^-$ ,  $A_2^-$ , and  $A_2^-$ , for the CMF, MF1, MF2, MF3, and MF4, respectively. In practice, for CMF, the  $\pi\pi$  interpolator is implemented with  $\mathbf{q} = -\mathbf{p}$  and  $\mathbf{p} = [0, 0, 1]$ . For the  $A_2^-$  and  $B_1^-$  irreducible representations of four MFs, the  $\pi\pi$  interpolators are all taken with  $\mathbf{q} = \mathbf{0}$ , and we calculate at four momenta,  $\mathbf{p} = [0, 0, 1]$ ,  $[1, 1, 0]$ ,  $[1, 1, 1]$  and  $[0, 0, 2]$  for each of the four moving frames, respectively.

In the isospin limit, topologically only six quark-line diagrams contribute to  $I = 1$   $\pi\pi$  scattering amplitudes, which are schematically illustrated in Fig. 1 of Ref. [11]. These diagrams are also elucidated in Fig. 1, where four pions are placed at lattice points  $x_1, x_2, x_3$ , and  $x_4$ , respectively [ $x_1 \equiv (\mathbf{x}_1, t_1)$ , etc.]. We usually label these diagrams as  $D$ ,  $X$ ,  $R_8$ ,  $R'_8$ ,  $R$ , and  $R'$  diagrams, respectively. The second diagram is also a kind of direct diagram; we call it  $X$  since its shape looks like an “X”. The shape of the third diagram looks like the number 8; thus, we use “ $R_8$ ” to identify it, which is also a kind of the rectangular diagram. The superscript prime in  $R$  and  $R_8$  indicates the corresponding counterclockwise partners.

The moving-wall source technique was initially introduced by Kuramashi *et al.* [23, 24] to study the  $I = 0, 2$   $\pi\pi$  scattering in the center-of-mass frame. Recently, we further extended this technique to the two-particle system with nonzero momenta to tentatively investigate the scalar  $\kappa$ ,  $\sigma$ , and vector  $K^*(892)$  meson decays [25]. In the present study, we use this technique to calculate the  $I = 1$   $\pi\pi$  scattering amplitudes by computing each  $T$  quark propagator corresponding to the moving-wall source at all the time slices [23–25],

$$\sum_{n'} D_{n, n'} G_t^{\mathbf{p}}(n') = \sum_{\mathbf{x}} \delta_{n, (\mathbf{x}, t)}, \quad 0 \leq t \leq T-1,$$

where  $D$  is the Dirac quark matrix, the subscript  $t$  in the quark propagator  $G$  indicates the temporal position of the wall source [23–25], and the superscript  $\mathbf{p}$  in  $G$  suggests that for the specified momentum  $\mathbf{p}$ , we select an

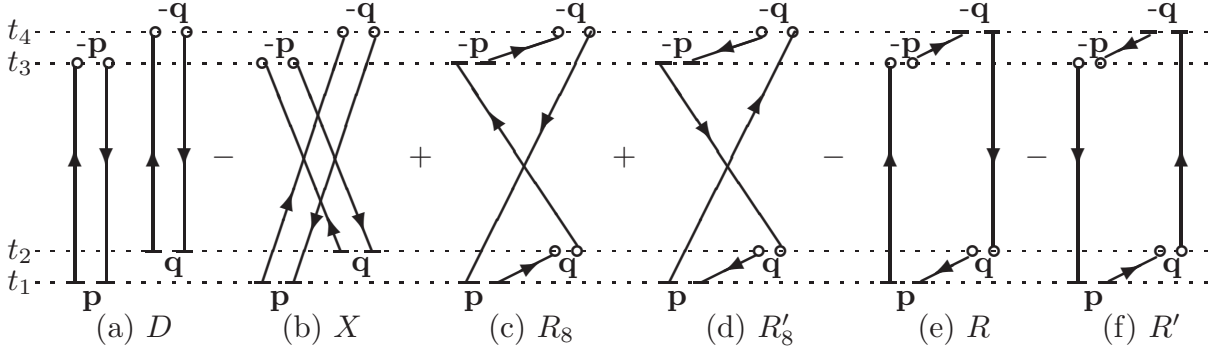


FIG. 1. (color online). Quark-link diagrams contributing to the  $I = 1$   $\pi\pi$  four-point functions. Short black bars stand for the wall sources. Open circles are sinks for local pion operators. The time flows upward in the diagrams. The pion operators are given with a momentum specified in the diagram.

up-quark source or sink with  $e^{i\mathbf{p}\cdot\mathbf{x}}$  (while an up-antiquark source or sink with 1) on each lattice site  $\mathbf{x}$  for the pion creation operator [25, 36, 37]. The associations of the quark propagators  $G_t^{\mathbf{p}}(n)$  exploiting the  $I = 1$   $\pi\pi$  four-

point correlation functions are schematically illustrated in Fig. 1 [23–25]. In terms of the quark propagators  $G_t^{\mathbf{p}}(n)$ , the  $D$ ,  $X$ ,  $R_8$ ,  $R_8'$ ,  $R$  and  $R'$  quark-line diagrams can be represented as

$$\begin{aligned}
C_{\pi\pi}^D(\mathbf{p}, \mathbf{q}; t_4, t_3, t_2, t_1) &= \sum_{\mathbf{x}_3} \sum_{\mathbf{x}_4} e^{-i(\mathbf{p}\cdot\mathbf{x}_3 + \mathbf{q}\cdot\mathbf{x}_4)} \langle \text{Tr}[G_{t_1}^\dagger(\mathbf{x}_3, t_3) G_{t_1}^{\mathbf{p}}(\mathbf{x}_3, t_3)] \text{Tr}[G_{t_2}^\dagger(\mathbf{x}_4, t_4) G_{t_2}^{\mathbf{q}}(\mathbf{x}_4, t_4)] \rangle, \\
C_{\pi\pi}^X(\mathbf{p}, \mathbf{q}; t_4, t_3, t_2, t_1) &= \sum_{\mathbf{x}_3} \sum_{\mathbf{x}_4} e^{-i(\mathbf{p}\cdot\mathbf{x}_3 + \mathbf{q}\cdot\mathbf{x}_4)} \langle \text{Tr}[G_{t_1}^\dagger(\mathbf{x}_4, t_4) G_{t_1}^{\mathbf{p}}(\mathbf{x}_4, t_4)] \text{Tr}[G_{t_2}^\dagger(\mathbf{x}_3, t_3) G_{t_2}^{\mathbf{q}}(\mathbf{x}_3, t_3)] \rangle, \\
C_{\pi\pi}^{R_8}(\mathbf{p}, \mathbf{q}; t_4, t_3, t_2, t_1) &= \sum_{\mathbf{x}_2} \sum_{\mathbf{x}_4} e^{i\mathbf{q}\cdot(\mathbf{x}_2 - \mathbf{x}_4)} \langle \text{Tr}[G_{t_1}^{\mathbf{p}}(\mathbf{x}_2, t_2) G_{t_3}^\dagger(\mathbf{x}_2, t_2) G_{t_3}^{-\mathbf{p}}(\mathbf{x}_4, t_4) G_{t_1}^\dagger(\mathbf{x}_4, t_4)] \rangle, \\
C_{\pi\pi}^{R_8'}(\mathbf{p}, \mathbf{q}; t_4, t_3, t_2, t_1) &= \sum_{\mathbf{x}_2} \sum_{\mathbf{x}_4} e^{i\mathbf{q}\cdot(\mathbf{x}_2 - \mathbf{x}_4)} \langle \text{Tr}[G_{t_3}^{-\mathbf{p}}(\mathbf{x}_2, t_2) G_{t_1}^\dagger(\mathbf{x}_2, t_2) G_{t_1}^{\mathbf{p}}(\mathbf{x}_4, t_4) G_{t_3}^\dagger(\mathbf{x}_4, t_4)] \rangle, \\
C_{\pi\pi}^R(\mathbf{p}, \mathbf{q}; t_4, t_3, t_2, t_1) &= \sum_{\mathbf{x}_2} \sum_{\mathbf{x}_3} e^{i(\mathbf{q}\cdot\mathbf{x}_2 - \mathbf{p}\cdot\mathbf{x}_3)} \langle \text{Tr}[G_{t_1}^{\mathbf{p}}(\mathbf{x}_3, t_3) G_{t_4}^\dagger(\mathbf{x}_3, t_3) G_{t_4}^{-\mathbf{q}}(\mathbf{x}_2, t_2) G_{t_1}^\dagger(\mathbf{x}_2, t_2)] \rangle, \\
C_{\pi\pi}^{R'}(\mathbf{p}, \mathbf{q}; t_4, t_3, t_2, t_1) &= \sum_{\mathbf{x}_2} \sum_{\mathbf{x}_3} e^{i(\mathbf{q}\cdot\mathbf{x}_2 - \mathbf{p}\cdot\mathbf{x}_3)} \langle \text{Tr}[G_{t_1}^{\mathbf{p}}(\mathbf{x}_2, t_2) G_{t_4}^\dagger(\mathbf{x}_2, t_2) G_{t_4}^{-\mathbf{q}}(\mathbf{x}_3, t_3) G_{t_1}^\dagger(\mathbf{x}_3, t_3)] \rangle, \tag{11}
\end{aligned}$$

where the traces are carried out over the color index, and the  $\gamma_5$ -Hermiticity nature of the light quark propagator  $G$ , *i.e.*,  $G(t, t')^\dagger = \gamma_5 G(t', t) \gamma_5$ , has been applied [23, 24].

According to the discussions in Ref. [17], in the isospin limit, the real parts of the third and fourth quark-line diagrams in Fig. 1 have the same values, while the corresponding imaginary parts have the same magnitudes as well, just with the opposite sign (likewise for the fifth and sixth quark-line diagrams).<sup>2</sup> Therefore, the value of the  $I = 1$   $\pi\pi$  four-point correlation function is purely real. Consequently, only four quark-line diagrams ( $D$ ,  $X$ ,  $R_8$ ,

and  $R$ ) are needed to calculate the  $I = 1$   $\pi\pi$  four-point correlation function, namely,

$$\begin{aligned}
C_{\pi\pi}(\mathbf{p}, \mathbf{q}; t) &\equiv \langle \mathcal{O}_{\pi\pi}(\mathbf{p}, \mathbf{q}; t) | \mathcal{O}_{\pi\pi}(\mathbf{p}, \mathbf{q}; 0) \rangle \\
&= D - X + 2N_f R_8 - 2N_f R, \tag{12}
\end{aligned}$$

where the staggered-flavor factor  $N_f$  should be inserted into the rectangular diagrams ( $R$  and  $R_8$ ) to amend for the additional factor  $N_f$  in the valence fermion loops [38]. We should remark at this point that the fourth-root recipes are supposed to correctly recover the right continuum limit of QCD [39].

## 2. $\rho$ sector

In principle, we can measure the propagators for two local  $\rho$  mesons,  $\gamma_i \otimes \gamma_i$  (VT) and  $\gamma_0 \gamma_i \otimes \gamma_0 \gamma_i$  (PV) [36, 37]. Nonetheless, we merely present lattice results for the

<sup>2</sup> This is true for the average with respect to the gauge configurations [17]. Note that this is true even for calculations at a single gauge configuration because the moving-wall source technique, a nonstochastic method, is used. This can be readily verified from the analytical expression in Eq. (11), where the random numbers are not used in these expressions.

local VT  $\rho$  meson because it gives more stable signals [36, 37]. Additionally, the numerical calculation of the three-point correlation function  $\rho \rightarrow \pi\pi$  is rather simple to compute if the local VT  $\rho$  interpolator is used. Therefore, we only employ an interpolator with isospin  $I = 1$  and  $J^P = 1^-$  at source and sink,

$$\mathcal{O}(x) \equiv \sum_c \frac{1}{\sqrt{2}} \{u_c(x)\gamma_i \otimes \gamma_i \bar{u}_c(x) - d_c(x)\gamma_i \otimes \gamma_i \bar{d}_c(x)\},$$

where  $c$  is the color index, and the subscript  $i$  in  $\gamma_i$  indicates the polarizations of the  $\rho$  vector current.

In the isospin limit, the disconnected quark-line diagrams for the  $\rho$  meson are nicely canceled out; consequently, the correlator for the neutral  $\rho$  meson in the momentum  $\mathbf{p}$  state is solely computed by the connected diagram

$$C_\rho(\mathbf{p}, t) = \sum_{\mathbf{x}} \sum_{a,b} e^{i\mathbf{p}\cdot\mathbf{x}} \langle u_b(\mathbf{x}, t)\gamma_i \otimes \gamma_i \bar{u}_b(\mathbf{x}, t) \times u_a(\mathbf{0}, 0)\gamma_i \otimes \gamma_i \bar{u}_a(\mathbf{0}, 0) \rangle,$$

where  $\mathbf{0}, \mathbf{x}$  are lattice spatial points of  $\rho$  states at the source and sink, respectively. In practice, we use the wall-source and point-sink interpolators to efficiently reduce the overlap with the excited states [40].

We fit the  $\rho$  correlator with the physical model as

$$C_\rho(t) = A \cosh\left[m\left(t - \frac{T}{2}\right)\right] + A'(-1)^{t+1} \cosh\left[m'\left(t - \frac{T}{2}\right)\right],$$

where  $A$  and  $A'$  are two overlap amplitudes, where only one mass is taken with each parity [36, 37, 41], and the oscillating parity partner is the  $p$ -wave meson with  $J^P = 1^+$ .

### 3. Off-diagonal sector

When studying the resonance parameters of the  $\rho$  meson [4–6, 11–22], one chiefly employs the stochastic method or its variants to measure the three-point function [42], which are successfully recently measured with the moving-wall source technique [25]. To hinder the twisted color Fierz transformation of the quark lines [24], we commonly choose  $t_1 \neq t_2$ . In practice, we pick  $t_1 = 0, t_2 = 1$ , and  $t_3 = t$  for the  $\pi\pi \rightarrow \rho$  three-point correlation function, and select  $t_1 = 0, t_2 = t$ , and  $t_3 = t + 1$  for the  $\rho \rightarrow \pi\pi$  three-point correlation function. The quark-line diagrams corresponding to the  $\rho \rightarrow \pi\pi$  and  $\pi\pi \rightarrow \rho$  are schematically illustrated in Figs. 2(a) and 2(b), respectively.

In practice, we employ an up-antiquark source with 1 on each lattice site  $\mathbf{x}$  for pion creation operator, and an up-quark source with  $e^{i\mathbf{p}\cdot\mathbf{x}}$  on each lattice site  $\mathbf{x}$  for pion creation operator [25]. It should be worthwhile to stress that the imaginary part of the second diagram for  $\pi\pi \rightarrow \rho$  should have same magnitude but with the minus sign, as that of the first diagram [17] (likewise for  $\rho \rightarrow \pi\pi$ ). As a consequence, the three-point diagrams are purely

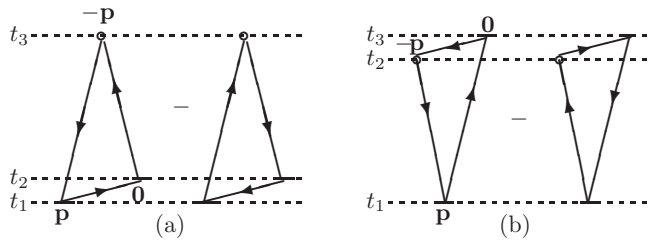


FIG. 2. (color online). Quark-link diagrams contributing to  $\pi\pi \rightarrow \rho$  and  $\rho \rightarrow \pi\pi$  three-point correlation functions. Short black bars indicate the wall sources. (a) Quark contractions of  $\pi\pi \rightarrow \rho$ , where the open circle is the sink for  $\rho$  operator. (b) Quark contractions of  $\rho \rightarrow \pi\pi$ , where the open circle is the sink for pion operator.

imaginary, and only one quark-line diagram is required to calculate each of the three-point correlation functions. We then write each of the first diagrams for the  $\rho \rightarrow \pi\pi$  and  $\pi\pi \rightarrow \rho$  quark-line diagrams in Fig. 2 in terms of the light quark propagators  $G$ ,

$$C_{\pi\pi \rightarrow \rho}(\mathbf{p}; t_3, t_2, t_1) = \sum_{\mathbf{x}_3, \mathbf{x}_2} e^{i\mathbf{p}\cdot\mathbf{x}_3} \langle \text{Tr}[G_{t_2}(\mathbf{x}_3, t_3)\gamma_5 G_{t_1}^\dagger(\mathbf{x}_3, t_3)\gamma_i G_{t_1}(\mathbf{x}_2, t_2)]\gamma_5 \rangle, \\ C_{\rho \rightarrow \pi\pi}(\mathbf{p}; t_3, t_2, t_1) = \sum_{\mathbf{x}_2, \mathbf{x}_3} e^{i\mathbf{p}\cdot\mathbf{x}_2} \langle \text{Tr}[G_{t_3}(\mathbf{x}_2, t_2)\gamma_i G_{t_1}^\dagger(\mathbf{x}_2, t_2)\gamma_5 G_{t_1}(\mathbf{x}_3, t_3)]\gamma_5 \rangle,$$

where the trace is taken over the color index and the Dirac matrix is used as an interpolator for the  $i$ th meson: the  $\gamma_5$  for the pseudoscalar meson and  $\gamma_i$  for the vector  $\rho$  meson, where the subscript  $i$  in the  $\gamma_i$  indicates the polarization of the  $\rho$  vector current.

### 4. Extraction of energies

To map out the avoided level crossings between the  $\rho$  resonance and its decay products, the variational method [9] is applied to separate the ground state from the first excited state. In practice, we calculate  $2 \times 2$  correlation function matrix  $C(t)$  denoted in (9), and construct a ratio of the correlation function matrices as

$$M(t, t_R) = C(t) C^{-1}(t_R), \quad (13)$$

with some reference time  $t_R$  [9] to extract two energy eigenvalues  $\bar{E}_n$  ( $n = 1, 2$ ), which can be obtained by a cosh fit to two eigenvalues  $\lambda_n(t, t_R)$  ( $n = 1, 2$ ) of the correlation matrix  $M(t, t_R)$  [43]

$$\lambda_n(t, t_R) = A_n \cosh\left[-E_n\left(t - \frac{T}{2}\right)\right] + (-1)^t B_n \cosh\left[-E'_n\left(t - \frac{T}{2}\right)\right]. \quad (14)$$

Note that the relevant higher correction is discussed in Ref. [35]. In practice, we will remove the “wraparound” contamination [44–47] before fitting with this formula.

TABLE II. Simulation parameters of the MILC gauge configurations. Lattice dimensions are described in lattice units with spatial ( $L$ ) and temporal ( $T$ ) size. The gauge coupling  $\beta$  is shown in Column 3. The fourth block give bare masses of the light and strange quark masses in terms of  $am_l$  and  $am_s$ , respectively. Column 5 gives pion masses in MeV. The lattice spatial dimension ( $L$ ) in fm and in units of the finite-volume pion mass are given in Column 6 and 7 respectively. We also list the mass ratio  $m_\pi/m_\rho$ . The number of time slices calculated  $\pi\pi$  correlators and  $\rho$  propagators for each of the lattice ensembles are shown in Column 9 and 11, respectively, and the last Column gives the number of gauge configurations used in this work.

Ensemble	$L^3 \times T$	$\beta$	$am_l/am_s$	$m_\pi(\text{MeV})$	$L(\text{fm})$	$m_\pi L$	$m_\pi/m_\rho$	$N_{\text{slice}}^{\pi\pi}$	$N_{\text{slice}}^\rho$	$N_{\text{cfg}}$
$a \approx 0.09$ fm										
6496f21b7075m00155m031	$64^3 \times 96$	7.075	0.00155/0.031	176	5.4	4.80	0.224	96	48	60
4096f21b708m0031m031	$40^3 \times 96$	7.08	0.0031/0.031	247	3.4	4.21	0.297	96	48	400
4096f3b7045m0031	$40^3 \times 96$	7.045	0.0031/0.0031	248	3.4	4.20	0.303	96	48	400
3296f21b7085m00465m031	$32^3 \times 96$	7.085	0.00465/0.031	301	2.7	4.11	0.312	96	48	400
2896f21b709m0062m031	$28^3 \times 96$	7.09	0.0062/0.031	346	2.4	4.14	0.380	96	48	400
$a \approx 0.12$ fm										
3264f3b6715m005	$32^3 \times 64$	6.715	0.005/0.005	275	3.7	5.15	0.299	64	32	637

### III. LATTICE CALCULATION

We employed the MILC gauge configurations with three Asqtad-improved staggered sea quarks [29, 30]. The simulation parameters are summarized in Table II. By MILC convention, lattice ensembles are referred to as “coarse” for the spatial lattice spacing  $a \approx 0.12$  fm, and “fine” for  $a \approx 0.09$  fm. It is handy to adopt  $(am_l, am_s)$  to classify MILC lattice ensembles. The conjugate gradient method is exploited to calculate the light quark propagators. We should remember that the MILC gauge configurations are generated using the staggered formulation of lattice the fermions [48] with the fourth root of fermion determinant [36]. All the gauge configurations were gauge fixed to the Coulomb gauge before calculating the light quark propagators.

To compute the  $\pi\pi$  four-point functions, the standard conjugate gradient method is adopted to get the necessary matrix element of the inverse Dirac fermion matrix, and the periodic boundary condition is applied to both the spatial and temporal directions. We compute the correlators on all the time slices, and explicitly combine the results from all the time slices  $T$ ; namely, the diagonal correlator  $C_{11}(t)$  is measured through

$$C_{11}(t) = \frac{1}{T} \sum_{t_s=0}^T \langle (\pi\pi)(t+t_s) (\pi\pi)^\dagger(t_s) \rangle.$$

After averaging the propagators over all the  $T$  values, the statistics are found to be remarkably improved.

For another diagonal correlator  $C_{22}(t)$ , the  $\rho$  correlator, we calculate

$$C_{22}(t) = \frac{2}{T} \sum_{t_s=0,2,4,\dots}^T \langle \rho^\dagger(t+t_s) \rho(t_s) \rangle,$$

where we sum the correlator over all the even time slices and average it.

According to the discussion in the Appendix, the noise-to-signal ratio of the  $\rho$  correlator and  $\pi\pi$  correlator are improved as approximately  $\propto \frac{1}{\sqrt{N_{\text{slice}} L^3}}$ , where  $L$  is the lattice spatial dimension and  $N_{\text{slice}}$  is the number of the time slices calculated the propagators for each of the gauge configurations. In this work, we use the lattice ensembles with relatively large  $L$  and sum the  $\rho$  correlator over all the even time slices and the  $\pi\pi$  correlator over all the time slices; consequently, it is natural that the signals of the correlators should be significantly improved. Admittedly, the most efficient way to improve the relevant noise-to-signal ratio is to use finer gauge configurations or anisotropic gauge configurations [18, 19]. See the Appendix for more details.

We evaluate the first off-diagonal correlator  $C_{21}(t)$ , the  $\pi\pi \rightarrow \rho$  three-point function, through

$$C_{21}(t) = \frac{1}{T} \sum_{t_s}^T \langle \rho(t+t_s) (\pi\pi)^\dagger(t_s) \rangle,$$

where the summation is over all the time slice. Due to the time-reversal symmetry [17], we can in practice merely calculate  $C_{21}^*(t)$ . By the relation  $C_{12}(t) = C_{21}^*(t)$ , we can freely get the second off-diagonal correlator  $C_{12}(t)$ .

We measure two-point pion correlators with the zero and nonzero momenta ( $\mathbf{0}$  and  $\mathbf{p}$ ) as well,

$$C_\pi(\mathbf{0}, t) = \frac{1}{T} \sum_{t_s=0}^{T-1} \langle 0 | \pi^\dagger(\mathbf{0}, t+t_s) W_\pi(\mathbf{0}, t_s) | 0 \rangle, \quad (15)$$

$$C_\pi(\mathbf{p}, t) = \frac{1}{T} \sum_{t_s=0}^{T-1} \langle 0 | \pi^\dagger(\mathbf{p}, t+t_s) W_\pi(\mathbf{p}, t_s) | 0 \rangle, \quad (16)$$

where  $\pi$  is the pion point-source operator and  $W_\pi$  is the pion wall-source operator [36, 37]. To simplify notation, the summation over the lattice space point in sink is not written out. It is worth noting that the summations over all the time slices for  $\pi$  propagators guarantee the extraction of the pion mass with high precision.

Disregarding the contributions from the excited states, the pion mass  $m_\pi$  and energy  $E_\pi(\mathbf{p})$  can be robustly extracted at large  $t$  from the two-point pion correlators (15) and (16), respectively [30],

$$C_\pi(\mathbf{0}, t) = A_\pi(\mathbf{0}) \left[ e^{-m_\pi t} + e^{-m_\pi(T-t)} \right] + \dots, \quad (17)$$

$$C_\pi(\mathbf{p}, t) = A_\pi(\mathbf{p}) \left[ e^{-E_\pi(\mathbf{p})t} + e^{-E_\pi(\mathbf{p})(T-t)} \right] + \dots, \quad (18)$$

where the ellipses show the oscillating parity partners, and  $A_\pi(\mathbf{0})$  and  $A_\pi(\mathbf{p})$  are two overlapping amplitudes, which will be subsequently exploited to estimate the wraparound contributions for  $I = 1$   $\pi\pi$  correlators [44–46].

## IV. LATTICE SIMULATION RESULTS

### A. Pion mass and dispersion relation

For each of the lattice ensembles, the pion masses  $m_\pi$  and energies  $E_\pi(\mathbf{p})$  were cautiously selected by seeking a combination of a plateau in the mass (or energy) as a function of the minimum fitting distances a  $D_{\min}$  [36, 37], fit quality, and  $D_{\min}$  large enough to efficiently suppress the excited states [40, 45]. For example, Fig. 3 exhibits the fit results of the pion masses or pion energies in lattice units as a function of  $D_{\min}$  for the (0.005, 0.005) ensemble. It is interesting and important to note that the rapid relaxations to the ground state for all of the five momenta, typically at or before  $t = 9$  from the source, indicates the feasibility of the wall-source and point-sink pion interpolators.

The lattice-measured values of the pion masses  $m_\pi$  and pion energies  $E_\pi(\mathbf{p})$  in lattice units, along with the fit ranges and fit qualities, are tabulated in Table III. The overlapping amplitudes  $A_\pi(\mathbf{0})$  or  $A_\pi(\mathbf{p})$  denoted in Eqs. (17) and (18) are also listed in Table III; these are later used to estimate the wraparound pollution to the  $I = 1$   $\pi\pi$  four-point correlators [44–46]. Note that the ETMC Collaboration reduces this unwanted lattice wraparound artifact by choosing the maximum time of the fit range to be far enough from the temporal boundaries [13]. In the present work, our measured quantities from these two-point functions are sufficiently precise to allow us to subtract the wraparound contributions.

The rho masses  $m_\rho$  are extracted from the  $\rho$  correlator, and the mass ratios of  $m_\pi/m_\rho$  are listed in Table II. It is important to note that our lattice-measured pion masses and the mass ratios of  $m_\pi/m_\rho$  turn out to be in good agreement with the corresponding MILC determinations [30, 36, 37, 49]. Note that our simulations are all carried out at physical kinematics  $m_\pi/m_\rho < 1/2$ .

It is interesting and important to note that the pion mesons on the lattice are found to have a continuum-like dispersion relation, as already observed in Ref. [50]. Say more specifically, for  $\mathbf{n}^2 < 4$ , our lattice-measured pion energies  $E_\pi(\mathbf{p} = \frac{2\pi}{L}\mathbf{n})$  are in good keeping with the

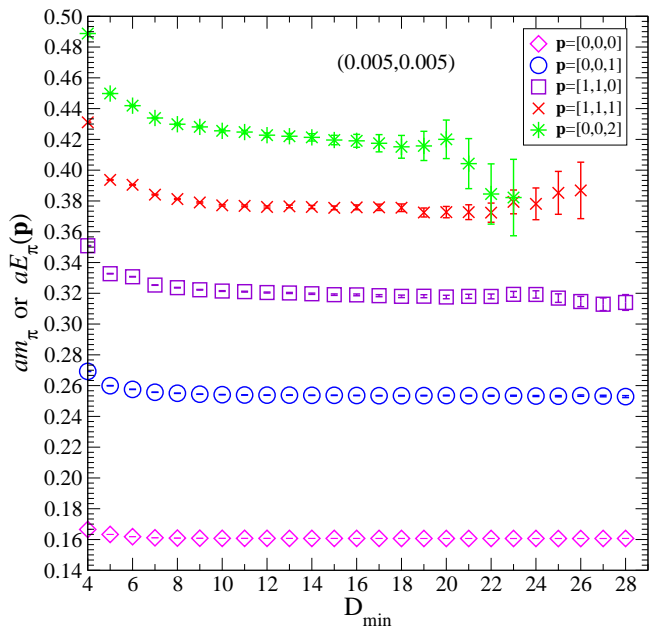


FIG. 3. (color online). Effective pion mass  $m_\pi$  or energy  $E_\pi(\mathbf{p})$  plots as the functions of  $D_{\min}$  for the (0.005, 0.005) ensemble. The plateaus are quickly reached typically at or before  $t = 8$  from the source.

continuum dispersion relation

$$E_{\text{cont}}(\mathbf{p}) = \sqrt{m_\pi^2 + |\mathbf{p}|^2} \quad (19)$$

within the errors, and are better than those evaluated with the prediction of the free lattice theory

$$aE_{\text{lat}} = \cosh^{-1} \left[ \cosh(am_\pi) + 2 \sum_i \sin^2 \left( \frac{1}{2} ap_i \right) \right], \quad (20)$$

where  $p = |\mathbf{p}|$  is the magnitude of each pion's scattering momentum in the center-of-mass frame. This is probably because the rotational invariance properties are improved due to the hypercubic smearing of the gauge link and quark operators [50].<sup>3</sup>

Note that for  $\mathbf{n}^2 = 4$  (i.e.,  $\mathbf{p} = [0, 0, 2]$ ), our lattice-measured pion energies  $E_\pi(\mathbf{p})$  for the (0.0031, 0.031) [ $L = 40$ ], (0.0031, 0.0031) [ $L = 40$ ], (0.00465, 0.031) [ $L = 32$ ] and (0.005, 0.005) [ $L = 32$ ] ensembles are well consistent with the continuum dispersion relation (19), whilst, those of the (0.0062, 0.031) [ $L = 28$ ] ensemble only barely meet the continuum dispersion relation (19). For this reason, we ignore the calculations relevant to the momentum  $\mathbf{p} = [0, 0, 2]$  for the (0.0062, 0.031) ensemble.

<sup>3</sup> This is also probably due to the significant improvement of the signal of the pion propagator as the pion momentum increases with large-enough  $L$  [27, 28]. As previously explained, the noise-to-signal ratio  $R_{NS}(t)$  of the pion energy  $E_\pi(\mathbf{p} = \frac{2\pi}{L}\mathbf{n})$  usually grows exponentially as  $R_{NS}(t) \propto \frac{1}{\sqrt{L^3}} \exp \left( \sqrt{m_\pi^2 + \frac{4\pi^2}{L^2} \mathbf{n}^2} - m_\pi \right) t$ .



TABLE III. Summary of the pion masses  $am_\pi$  or pion energies  $aE_\pi(\mathbf{p})$  obtained from the pion propagators for six MILC lattice ensembles with four momenta,  $\mathbf{p} = [0, 0, 1]$ ,  $[1, 1, 0]$ ,  $[1, 1, 1]$ , and  $[0, 0, 2]$ . The lattice-measured pion energies  $aE_\pi(\mathbf{p})$  are compared with the analytical predictions from the continuum (19) and free lattice theory (20), where the uncertainties are estimated solely from the statistical errors of the lattice-measured  $am_\pi$ . The fifth block shows the overlapping amplitudes  $A_\pi(\mathbf{0})$  or  $A_\pi(\mathbf{p})$  denoted in Eqs. (17) and (18), respectively. The third and fourth blocks indicate the fit range, and fit quality  $\chi^2/\text{DOF}$ , respectively.

Ensemble	$\mathbf{n} = \mathbf{p}\frac{L}{2\pi}$	Range	$\chi^2/\text{DOF}$	$A_\pi(\mathbf{0})/A_\pi(\mathbf{p})$	$am_\pi/aE_\pi(\mathbf{p})$	$aE_{cont}$	$aE_{lat}$
(0.00155, 0.031)	(0, 0, 0)	33 – 48	14.1/12	$6603.86 \pm 4.84$	0.07501(6)	–	–
	(0, 0, 1)	19 – 45	26.1/21	$4136.59 \pm 7.49$	0.12348(14)	0.12355(6)	0.12345(6)
	(1, 1, 0)	16 – 42	18.4/23	$3035.31 \pm 12.73$	0.15793(19)	0.15780(5)	0.15760(4)
	(1, 1, 1)	15 – 40	26.2/22	$2324.42 \pm 16.12$	0.18579(24)	0.18585(4)	0.18553(4)
	(0, 0, 2)	13 – 36	23.6/20	$2055.65 \pm 18.74$	0.21023(36)	0.21019(4)	0.20951(4)
(0.0031, 0.0031)	(0, 0, 0)	30 – 47	15.8/14	$1091.62 \pm 1.73$	0.10505(6)	–	–
	(0, 0, 1)	19 – 48	23.9/26	$619.13 \pm 2.37$	0.18963(38)	0.18896(5)	0.18857(5)
	(1, 1, 0)	16 – 48	37.8/29	$482.97 \pm 3.24$	0.24709(95)	0.24572(4)	0.24493(4)
	(1, 1, 1)	13 – 36	29.2/20	$414.45 \pm 7.44$	0.2929(15)	0.29164(3)	0.29038(3)
	(0, 0, 2)	12 – 48	38.3/33	$381.03 \pm 7.93$	0.3343(18)	0.33125(3)	0.32856(3)
(0.0031, 0.031)	(0, 0, 0)	33 – 45	11.1/9	$1218.53 \pm 1.74$	0.10535(6)	–	–
	(0, 0, 1)	19 – 41	24.1/19	$684.89 \pm 1.89$	0.19016(21)	0.18916(6)	0.18875(6)
	(1, 1, 0)	16 – 36	16.4/17	$525.61 \pm 3.83$	0.24713(49)	0.24588(5)	0.24506(4)
	(1, 1, 1)	15 – 37	16.4/19	$431.92 \pm 6.32$	0.29124(105)	0.29177(4)	0.29049(4)
	(0, 0, 2)	13 – 34	22.6/18	$398.53 \pm 9.34$	0.33244(172)	0.33135(4)	0.32866(3)
(0.00465, 0.031)	(0, 0, 0)	30 – 48	10.3/15	$538.41 \pm 1.31$	0.12852(9)	–	–
	(0, 0, 1)	20 – 45	30.9/22	$292.55 \pm 2.32$	0.23513(46)	0.23465(10)	0.23390(10)
	(1, 1, 0)	17 – 43	28.2/23	$224.28 \pm 5.03$	0.3048(13)	0.30596(8)	0.30442(8)
	(1, 1, 1)	15 – 27	14.2/9	$197.07 \pm 6.46$	0.3643(23)	0.36355(6)	0.36110(6)
	(0, 0, 2)	13 – 24	10.6/8	$172.67 \pm 9.00$	0.4132(42)	0.41318(6)	0.40798(6)
(0.0062, 0.031)	(0, 0, 0)	30 – 48	24.3/15	$330.73 \pm 0.94$	0.14718(13)	–	–
	(0, 0, 1)	20 – 48	34.3/25	$179.83 \pm 2.31$	0.26751(72)	0.26837(14)	0.26725(14)
	(1, 1, 0)	17 – 42	22.7/22	$139.60 \pm 3.65$	0.3471(17)	0.34982(11)	0.34752(11)
	(1, 1, 1)	14 – 19	3.0/2	$126.23 \pm 4.27$	0.4170(26)	0.41561(9)	0.411987(9)
(0.005, 0.005)	(0, 0, 0)	20 – 32	6.8/9	$1717.95 \pm 1.66$	0.16068(5)	–	–
	(0, 0, 1)	14 – 32	22.4/15	$1091.01 \pm 1.96$	0.25371(13)	0.25373(3)	0.25292(3)
	(1, 1, 0)	13 – 30	23.4/13	$856.21 \pm 3.86$	0.32013(35)	0.32083(3)	0.31917(3)
	(1, 1, 1)	12 – 32	11.7/17	$737.78 \pm 6.11$	0.37610(71)	0.37614(2)	0.37355(2)
	(0, 0, 2)	11 – 32	22.6/18	$669.81 \pm 8.00$	0.42475(112)	0.42430(2)	0.41897(2)

In summary, the continuum dispersion relation (19) for the single pion state is valid up to the momentum  $\mathbf{p} = [0, 0, 2]$  within statistical errors [except for the (0.0062, 0.031) ensemble, the relevant results for which are not listed in Table III]. Consequently, we will use the continuum dispersion relation (19) throughout the remaining analysis. This means that the center-of-mass scattering momentum  $p^*$  is extracted from the lattice energy through the continuum dispersion relation, and the resulting  $p^*$  is used to extract the scattering phase shift. Additional relevant issues will be discussed in Sec. IV D. It is worth stressing that the robust measurements of the pion propagator with high momenta indeed guarantee reliable estimations of the  $\pi\pi$  propagator with high momenta.

## B. Finite- $T$ contributions for the $\pi\pi$ correlators

In this work,  $I = 1$   $\pi\pi$  energy spectra are meticulously secured from  $\pi\pi$  correlators, which are unavoidably impacted by the finite temporal extent of the lattice [44–47]. In principle, the size of the finite temporal effects can be estimated, and are slight on a typical lattice study. Nonetheless, these effects are large enough to be visible, particularly for the  $I = 1$   $\pi\pi$  correlators calculating with small quark masses [26]. Using the original notations in [47], we here briefly review the finite- $T$  effects on  $I = 1$   $\pi\pi$  correlators at rest (i.e., the total momentum of  $\pi\pi$  system  $\mathbf{P} = \mathbf{0}$ ) and those in flight (i.e.,  $\mathbf{P} \neq \mathbf{0}$ ).

Since the periodic boundary condition is enforced in the temporal direction, one of two pions can spread  $T - t$

time steps backwards, which leads to a pollution of the  $\pi\pi$  correlators at large  $t$  [44–46]. Additionally, in the isospin limit, two direct quark-line diagrams ( $D$  and  $X$ ) in Fig. 1 contribute to the  $I = 1$   $\pi\pi$  scattering amplitudes, and both of them have wraparound pollution. The wraparound pollution from the direct diagram  $D$  in the limit of weakly interacting pions, which is one pion with the momentum  $\mathbf{p}$ , and another pion with momentum  $\mathbf{q}$ , can be approximately estimated by [47]

$$\begin{aligned} \text{WP}(t) \approx & A_\pi(\mathbf{q})A_\pi(\mathbf{p}) \left( e^{-E_\pi(\mathbf{q})(T-t)} e^{-E_\pi(\mathbf{p})t} \right. \\ & \left. + e^{-E_\pi(\mathbf{p})(T-t)} e^{-E_\pi(\mathbf{q})t} \right), \end{aligned} \quad (21)$$

where the overlapping amplitudes  $A_\pi(\mathbf{p})$  denoted in (18), along with the pion masses  $m_\pi$  and pion energy  $E_\pi(\mathbf{p})$ , can be robustly extracted from the pion propagators. The undesired wraparound contributions to the  $I = 1$   $\pi\pi$  four-point correlators in the moving frame are generally time dependent [47]. The wraparound pollution of the direct diagram  $X$  in Fig. 1 can be analogously dealt with; therefore, we do not explicitly write it out.

As a simple example, considering the  $I = 1$   $\pi\pi$  correlators in CMF ( $\mathbf{q} = -\mathbf{p}$ ), this leads to a constant pollution

$$C(\mathbf{p}) = 2(A_\pi(\mathbf{p}))^2 e^{-E_\pi(\mathbf{p})T}, \quad (22)$$

where the overlapping amplitudes  $A_\pi(\mathbf{p})$ , and pion energy  $E_\pi(\mathbf{p})$  are summarized in Table III.

Considering another concrete example of the  $\pi\pi$  correlator with  $\pi^+(\mathbf{0})\pi^+(\mathbf{p})$  at the source and  $\pi^-(\mathbf{0})\pi^-(\mathbf{p})$  at the sink (this is one pion at rest, one pion with the momentum  $\mathbf{p}$ , and total momentum  $\mathbf{P} = \mathbf{p}$ ), the wanted contribution in the limit of weakly interacting pions can be approximately estimated by [47]

$$\approx A_\pi(\mathbf{0})A_\pi(\mathbf{p})e^{-(m_\pi+E_\pi(\mathbf{p}))t}, \quad (23)$$

where the overlapping amplitudes  $A_\pi(\mathbf{0})$  and  $A_\pi(\mathbf{p})$  are denoted in Eqs. (17) and (18), respectively. Meanwhile, the wraparound terms for this moving frame  $\text{WP}_{\text{MF}}(t)$  are evaluated by [47]

$$\begin{aligned} \text{WP}_{\text{MF}}(\mathbf{p}, t) \approx & A_\pi(\mathbf{0})A_\pi(\mathbf{p}) \left( e^{-m_\pi(T-t)} e^{-E_\pi(\mathbf{p})t} \right. \\ & \left. + e^{-E_\pi(\mathbf{p})(T-t)} e^{-m_\pi t} \right), \end{aligned} \quad (24)$$

where the first term is anticipated to lead the contamination for the time regions of interest [47]. Moreover, the largest pollution term is not a constant but rather has a time dependence  $\sim e^{-\Delta E_\pi t}$ , where  $\Delta E_\pi \equiv E_\pi(\mathbf{p}) - m_\pi$  is the positive energy gap between one pion with zero momentum and another with momentum  $\mathbf{p}$ . Besides, the second pollution term has a time dependence  $\sim e^{\Delta E_\pi t}$ . Note that the ratio of the first term to the second term is roughly proportional to  $e^{-\Delta E_\pi(T-2t)}$ , which indicates that both pollution terms significantly contribute the whole pollution on large times.

Since the impact of the finite- $T$  effects on the  $I = 1$   $\pi\pi$  correlators in flight is statistically significant [47], it is

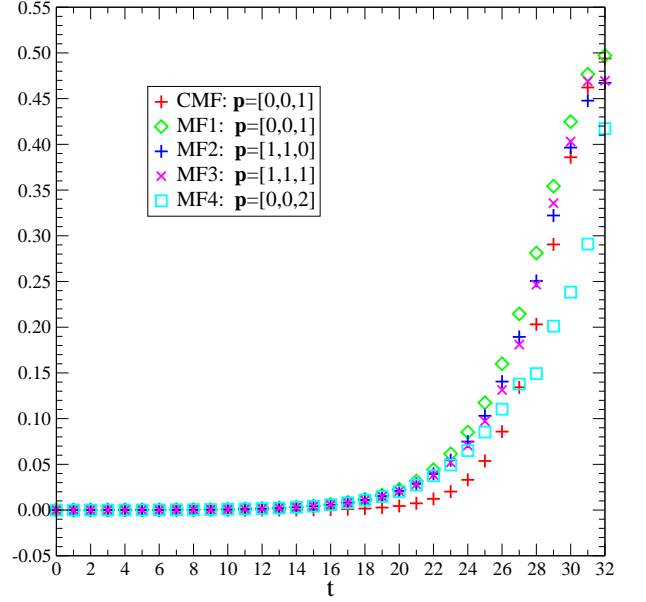


FIG. 4. (color online). Ratios of the wraparound pollution to the  $\pi\pi$  correlators of the direct diagram for the (0.005, 0.005) ensemble using Eq. (25) for four momenta,  $\mathbf{p} = [0, 0, 1]$ ,  $[1, 1, 0]$ ,  $[1, 1, 1]$ , and  $[0, 0, 2]$ , along with the ratio for the center-of-mass frame at  $\mathbf{p} = [0, 0, 1]$ . These ratios are generally near 1/2 as  $t$  approaches  $T/2$  as anticipated from the analytical statements in Refs. [44–47].

necessary to correct these terms in the variational analysis of the in-flight  $\pi\pi$  spectra. In practice, we subtract all the pollution terms in Eq. (24) from the  $\pi\pi$  correlators. This turns out to be a rather good approximation for the lattice simulation in this work.

In order to comprehend this finite- $T$  effect at a quantitative level, we denote a quantity

$$R_{\text{MF}}(\mathbf{p}, t) = \frac{\text{WP}_{\text{MF}}(\mathbf{p}, t)}{D_{\pi\pi}^{I=1}(\mathbf{p}, t)}, \quad (25)$$

which is the ratio of the finite- $T$  effect  $\text{WP}_{\text{MF}}(\mathbf{p}, t)$  calculated by Eq. (24) to the  $I = 1$   $\pi\pi$  correlator  $D_{\pi\pi}^{I=1}(\mathbf{p}, t)$  of the direct diagram  $D$ . In Fig. 4, we illustrate this ratio for the (0.005, 0.005) ensemble at four momenta,  $\mathbf{p} = [0, 0, 1]$ ,  $[1, 1, 0]$ ,  $[1, 1, 1]$ , and  $[0, 0, 2]$ , together with the ratio for the center-of-mass frame, which is denoted by

$$R_{\text{CM}}(\mathbf{p}, t) = C(\mathbf{p})/D_{\pi\pi}^{I=1}(\mathbf{p}, t)$$

for  $\mathbf{p} = [0, 0, 1]$ , where  $C(\mathbf{p})$  is defined in Eq. (22). These ratios turn out to make a significant contribution to  $\pi\pi$  correlators as  $t$  approaches  $T/2$  [44–47]. Consequently, it is required to explicitly account for this pollution when extracting the  $\pi\pi$  energy. Through appropriately subtracting this effect from the  $\pi\pi$  correlators, these unwanted finite- $T$  effects are anticipated to be neatly removed. The relevant ratios for the (0.005, 0.005) ensemble are illustrated in Fig. 5. It is interesting to note that the wraparound pollution generally contributes in relatively smaller quantities for the higher momenta.

### C. Energy eigenvalues

The finite- $T$  effects for  $\pi\pi$  correlators at rest are constant in time, while those in flight are generally time-dependent. It is natural to explicitly incorporate these wraparound terms for a successful energy spectral fit of  $\pi\pi$  correlators. In the present study, these wraparound effects can be accurately estimated and consequently, can be appropriately subtracted from the corresponding  $I = 1$   $\pi\pi$  correlators. After deducting these undesired effects, the remaining  $I = 1$   $\pi\pi$  correlators then hold clean information.

As practised in Refs. [25], we calculate two eigenvalues  $\lambda_n(t, t_R)$  ( $n = 1, 2$ ) for the matrix  $M(t, t_R)$  denoted in Eq. (13) with the reference time  $t_R$ . By defining a fit range  $[t_{\min}, t_{\max}]$  and adjusting the minimum fitting distance  $t_{\min}$  and maximum fitting distance  $t_{\max}$ , we can acquire energy levels from  $\lambda_n(n = 1, 2)$  in a correct manner. In this work, we take  $t_{\min} = t_R + 1$  [13]; in order to extract the desired energies  $\overline{E}_n(t_{\min})$  ( $n = 1, 2$ ), two eigenvalues  $\lambda_n(t, t_R)$  ( $n = 1, 2$ ) at the chosen  $t_{\min}$  were fit to Eq. (14), with the  $t_{\max}$  either at  $T/2$  or where the fractional statistical errors exceeded about 20% for two successive time slices. Examples of fitted energy levels as functions of  $t_{\min}$  for the nine energy states with the relevant representations considered in the present work are illustrated in Fig. 5 for the (0.005, 0.005) ensemble. The dotted lines in each panel indicate the energy levels of the two free pions for the relevant representation.

For each of the lattice ensembles, the energy levels  $\overline{E}_n(n = 1, 2)$  with the  $\mathbf{A}_2^-$ ,  $\mathbf{B}_1^-$ ,  $\mathbf{A}_2^-$ , and  $\mathbf{A}_2^-$  representations for the MF1, MF2, MF3, and MF4, respectively, were carefully selected by seeking the combination of a plateau in the effective energy plots as the function of  $t_{\min}$  and a reasonable fit quality. The fit range and fit quality  $\chi^2/\text{DOF}$ , along with the fitted  $\overline{E}_n$  ( $n = 1, 2$ ) for six MILC lattice ensembles, are summarized in Table IV. The lattice-measured energy levels  $\overline{E}_n$  ( $n = 1, 2$ ) are then employed to derive the  $p$ -wave scattering phase shifts  $\delta_1$  by the corresponding finite size formulas, which are summarized in Table IV. The relevant fitted results with the  $\mathbf{T}_1^-$  representation for CMF are also summarized in Table IV as well.<sup>4</sup>

It is worthwhile stressing that the finite-size effects are exponentially suppressed with the combination  $m_\pi L$ , which obviously decreases with the small  $am_\pi$ ; it is expensive to compensate for this with higher lattice spatial dimensions  $L$ . From Table II, we note that in the present study our lattice volumes all have  $m_\pi L > 4$ ; consequently, the finite-size effects are negligible, and the Lüscher formulas are perfectly satisfied [8, 9].

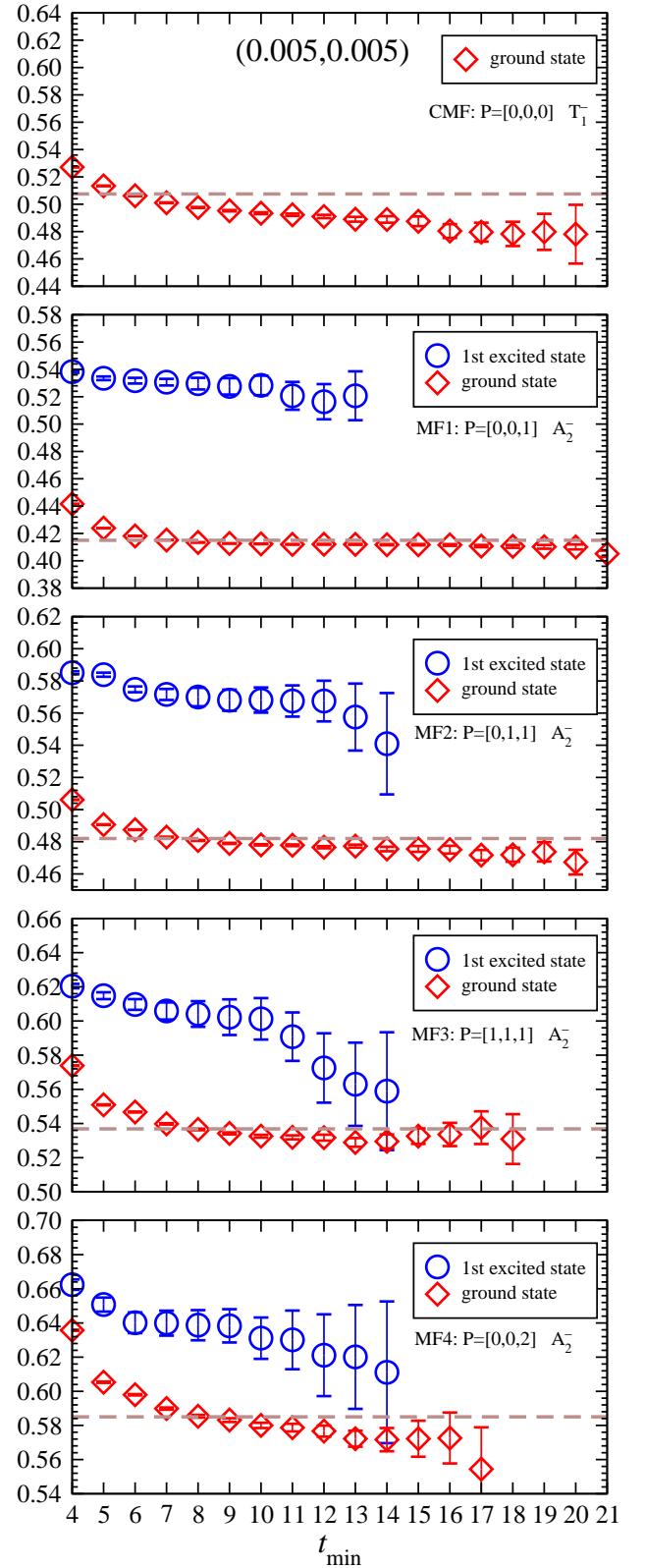


FIG. 5. Fitted energy levels as functions of  $t_{\min}$  for the ground states of the  $\mathbf{T}_1^-$  representation in CMF, and for the ground and first excited states of the  $\mathbf{A}_2^-$ ,  $\mathbf{B}_1^-$ ,  $\mathbf{A}_2^-$  and  $\mathbf{A}_2^-$  representations for MF1, MF2, MF3, and MF4, respectively, with the (0.005, 0.005) ensemble.

<sup>4</sup> The lattice determinations of the four-pion thresholds for the MFs and CMFs are generally discussed in Ref. [22]. Moreover, according to the discussions in Refs. [22, 51], the  $\rho$  meson to  $4\pi$  states is indeed negligible.

TABLE IV: Summaries of the fitted energy levels with the  $\mathbf{A}_2^-$  representation for the ground state ( $n = 1$ ) and first excited state ( $n = 2$ ) in MF1, MF2, MF3, and MF4, respectively, and the  $\mathbf{T}_1^-$  representation in CMF, for six lattice ensembles. The fit range ( $t_{\min}, t_{\max}$ ),  $\chi^2/\text{DOF}$ , and extracted energy levels  $E_n$  ( $n = 1, 2$ ) are tabulated in Column 4, 5, 6, respectively. The center-of-mass scattering momentum  $p^*$  and the invariant mass  $\sqrt{s}$  are obtained using the dispersion relations (26), and the relevant  $p$ -wave scattering phase  $\delta_1$  in units of degree is obtained by the corresponding finite-size formulas.

Ensemble	Frame	Level $n$	Fit range	$\chi^2/\text{DOF}$	$aE_n$	$a\sqrt{s}$	$ap^*$	$\delta_1(^{\circ})$	
(0.00155, 0.031)	CMF		21 – 40	21.5/16	0.2446(17)		0.00933(21)	6.0(3.9)	
	MF1	1	22 – 44	15.1/19	0.19779(21)	0.17170(24)	0.00174(2)	0.69(20)	
		2	9 – 34	26.4/22	0.3574(18)	0.3437(19)	0.02390(32)	100.4(8.1)	
	MF2	1	16 – 38	21.3/19	0.23190(32)	0.18575(40)	0.00300(4)	1.28(53)	
		2	8 – 20	9.6/9	0.3758(16)	0.3492(17)	0.02486(30)	103.5(6.9)	
	MF3	1	14 – 24	9.1/7	0.25950(48)	0.19602(64)	0.00398(6)	1.86(1.6)	
		2	8 – 18	8.2/7	0.3988(19)	0.3607(21)	0.02691(38)	132.8(4.1)	
	MF4	1	13 – 22	8.2/6	0.28404(71)	0.20525(98)	0.00490(10)	2.5(2)	
		2	8 – 18	7.2/7	0.4153(21)	0.3659(24)	0.02785(44)	131.59(5.3)	
	(0.0031, 0.0031)	CMF		22 – 48	28.2/23	0.3355(64)		0.0171(11)	53.6(7.2)
MF1		1	18 – 37	15.6/16	0.29003(40)	0.24381(48)	0.00383(6)	1.87(19)	
		2	9 – 35	20.7/23	0.3841(21)	0.3505(23)	0.01968(40)	96.8(2.8)	
MF2		1	15 – 40	20.8/22	0.34589(81)	0.26512(106)	0.00654(14)	3.81(75)	
		2	8 – 28	19.6/17	0.4214(23)	0.3581(27)	0.02103(48)	109.4(3.2)	
MF3		1	14 – 39	27.4/22	0.38929(133)	0.2784(19)	0.00835(26)	5.8(1.4)	
		2	8 – 22	13.2/11	0.4532(27)	0.3625(34)	0.02181(61)	123.9(4.6)	
MF4		1	12 – 38	13.7/23	0.4283(25)	0.2911(36)	0.01016(52)	9.7(4.2)	
		2	8 – 18	11.2/7	0.4807(36)	0.3639(48)	0.02207(87)	123.6(5.9)	
(0.0031, 0.031)		CMF		21 – 32	15.1/8	0.3423(61)		0.0182(10)	46.3(7.0)
	MF1	1	22 – 41	18.4/16	0.29134(62)	0.24543(75)	0.00395(9)	1.51(31)	
		2	9 – 32	19.5/20	0.3900(18)	0.3570(20)	0.0208(35)	89.4(2.5)	
	MF2	1	16 – 36	20.6/17	0.34632(99)	0.2657(13)	0.00655(17)	3.8(0.9)	
		2	8 – 20	8.8/9	0.4230(27)	0.3600(32)	0.02130(57)	107.8(3.8)	
	MF3	1	14 – 22	8.1/5	0.3899(15)	0.2786(21)	0.00830(29)	6.0(1.6)	
		2	8 – 18	8.0/7	0.4590(24)	0.3697(30)	0.02307(55)	116.3(4.3)	
	MF4	1	13 – 21	9.3/5	0.4288(17)	0.2918(25)	0.01019(36)	9.6(2.8)	
		2	7 – 17	10.1/7	0.4873(32)	0.3725(42)	0.02359(77)	115.0(5.3)	
	(0.00465, 0.031)	CMF		10 – 18	7.2/5	0.3769(61)		0.0190(15)	86.7(6.7)
MF1		1	15 – 35	28.6/17	0.3539(14)	0.2944(17)	0.00516(25)	3.09(40)	
		2	7 – 28	24.9/18	0.4381(26)	0.3916(29)	0.0218(6)	131.2(2.2)	
MF2		1	16 – 48	34.3/29	0.4214(42)	0.3170(56)	0.00862(88)	7.8(2.9)	
		2	7 – 27	29.8/17	0.4849(34)	0.3975(41)	0.0230(8)	144.2(3.1)	
MF3		1	15 – 36	22.1/18	0.4741(63)	0.3303(90)	0.0108(15)	11.5(6.2)	
		2	8 – 21	15.9/10	0.5203(44)	0.4070(57)	0.0249(12)	154.7(4.2)	
MF4		1	12 – 28	19.8/13	0.5219(56)	0.3438(86)	0.0130(15)	18.7(7.8)	
		2	8 – 20	14.7/9	0.5705(52)	0.4138(73)	0.0263(15)	152.0(6.6)	
(0.0062, 0.031)		CMF		17 – 48	34.5/28	0.397(11)		0.0177(23)	110.7(4.0)
	MF1	1	12 – 17	1.3/2	0.4018(12)	0.3333(13)	0.00611(23)	3.69(21)	
		2	7 – 20	13.0/10	0.4716(25)	0.4148(28)	0.02135(59)	150.6(1.7)	
	MF2	1	12 – 32	21.0/16	0.4766(40)	0.3559(51)	0.01001(91)	10.3(2.2)	
		2	7 – 17/	9.8/7	0.5367(48)	0.4328(60)	0.0252(13)	156.3(3.6)	
	MF3	1	13 – 21	5.9/5	0.5304(66)	0.3608(98)	0.0109(18)	20.2(8.0)	
		2	6 – 16/	8.4/7	0.5923(67)	0.4470(89)	0.0283(20)	163.7(5.0)	
	(0.005, 0.005)	CMF		18 – 24	2.9/3	0.4715(89)		0.0298(21)	40.4(9.2)
		MF1	1	11 – 18	2.7/4	0.41110(25)	0.36118(28)	0.00680(5)	1.49(12)
			2	8 – 18	8.2/7	0.5296(43)	0.4919(46)	0.0347(11)	80.0(5.6)
MF2		1	13 – 32	21.0/16	0.47659(65)	0.3873(8)	0.01169(16)	3.59(54)	
		2	8 – 23	14.1/12	0.5699(57)	0.4977(65)	0.0361(16)	100.4(6.9)	
MF3		1	13 – 18	0.9/2	0.5289(28)	0.4051(33)	0.0152(7)	5.7(2.3)	
		2	7 – 17	6.7/7	0.6058(50)	0.5013(62)	0.0370(15)	119.8(6.8)	
MF4		1	13 – 32	19.5/16	0.5727(46)	0.4169(62)	0.0176(13)	14.1(6.8)	
		2	7 – 17	8.6/7	0.6399(73)	0.5052(92)	0.0380(23)	116.0(10.3)	

### D. Finite-size effects

We employ the following relations:

$$\begin{aligned}\sqrt{s} &= \sqrt{E_{MF}^2 - P^{*2}}, \\ p^{*2} &= \frac{s}{4} - m_\pi^2,\end{aligned}\quad (26)$$

in the Lorentz transformation for the invariant mass  $\sqrt{s}$ , the energy of  $\pi\pi$  system in the moving frame  $E_{MF}$  and the center-of-mass scattering momentum  $p^*$ . Equation (26) is only suitable up to the truncation errors. Rummukainen and Gottlieb suggest [10]

$$\begin{aligned}\cosh(\sqrt{s}) &= \cosh(E_{MF}) - 2\sin^2\left(\frac{P^*}{2}\right), \\ 2\sin^2\left(\frac{p^*}{2}\right) &= \cosh\left(\frac{\sqrt{s}}{2}\right) - \cosh(m_\pi)\end{aligned}\quad (27)$$

to reduce this truncation error. Recently, we extended them to a two-particle system with arbitrary masses [25].

We discern no obvious difference of the ultimate results due to the selection of the energy momentum relations (26) or (27) within the statistics, especially for lattice ensemble with a smaller lattice space  $a$  or large spatial extent  $L$ . For these reasons, we computed the  $\sqrt{s}$  and  $p^*$  by the continuum relation (26).

## V. ANALYSIS

We are now in a position to use the scattering phases  $\delta_1$  to secure the  $\rho$  resonance parameters. Moreover, since we have six sets of lattice data at hand, we can follow the pioneering work of the ETMC Collaboration [13] to discuss the pion mass dependence on  $\rho$  resonance parameters. After chiral extrapolation to the physical point, the desired physical quantities can be obtained.

### A. Resonant parametrizations

To estimate the two-pion energies, we use the well-known effective range formula [1]

$$\tan \delta_1 = \frac{g_{\rho\pi\pi}^2}{6\pi} \frac{p^3}{\sqrt{s}(M_R^2 - s)}, \quad p = \sqrt{\frac{s}{4} - m_\pi^2}. \quad (28)$$

where the Mandelstam variable  $s$  is denoted by the center-of-mass energy of the  $\pi\pi$  system  $E_{CM}$  through  $s = E_{CM}^2$ . This enables a fit for two unknown quantities: the coupling constant  $g_{\rho\pi\pi}$  and the resonance mass  $M_R$  from the lattice-determined  $p$ -wave scattering phase  $\delta_1$ . The  $\rho$  decay width is then calculated through

$$\Gamma_\rho = \Gamma_R(s) \Big|_{s=M_R^2} = \frac{g_{\rho\pi\pi}^2}{6\pi} \frac{\left(\frac{M_R^2}{4} - m_\pi^2\right)^{3/2}}{M_R^2}. \quad (29)$$

Equations (28) and (29) offer us a way to acquire  $\rho$  range parameters by examining the dependence of  $\delta_1$  on  $\sqrt{s}$ .

### B. Extraction of the resonance parameters

For six MILC lattice ensembles, we obtained seven or nine separate energy levels, and we can then extract seven or nine  $p$ -wave scattering phases  $\delta_1$  from the relevant invariant mass  $\sqrt{s}$ ; these are shown in Fig. 6. To extract the resonance mass  $m_\rho$  and the coupling constant  $g_{\rho\pi\pi}$  from a single lattice ensemble, the seven or nine  $p$ -wave scattering phases  $\delta_1$  are then fitted with the effective range formula denoted in Eq. (28).<sup>5</sup> The corresponding fits for six lattice ensembles are also exhibited in Fig. 6. The fitted  $m_\rho$  in MeV and  $g_{\rho\pi\pi}$  are summarized in Table V, where the statistical errors of the lattice spacing  $a$  are also added in quadrature.

Once the fitted values of the  $g_{\rho\pi\pi}$  and  $m_\rho$  in lattice units are acquired, the decay width  $\Gamma_\rho$  in lattice units can be estimated by Eq. (29), where the uncertainties are solely estimated from the statistical errors of both  $g_{\rho\pi\pi}$  and  $am_\rho$ . The calculated  $\Gamma_\rho$  is also listed in Table V, where the statistical errors of the lattice spacing  $a$  are also added in quadrature. It is worth mentioning that  $\Gamma_\rho$  is mainly determined by the  $\pi\pi$ -phase space; consequently, this number derived from the different quark masses turns out to be different.<sup>6</sup> Note that the lattice-calculated  $\Gamma_\rho$  for the larger quark masses are significantly smaller than the experimental value quoted by the Particle Data Group (PDG)  $\Gamma_\rho^{\text{phys}} = 147.8(9)$  [1]. To make our demonstrations of these results more intuitive, the resonance masses and the resonance regions are offered graphically in Fig. 6.

TABLE V. Summary of the fitted  $\rho$ -meson mass  $m_\rho$  and the effective coupling constant  $g_{\rho\pi\pi}$  for the six MILC lattice ensembles. The relevant estimated decay widths  $\Gamma_\rho$  are also listed, where the statistical errors of the lattice spacing  $a$  are also considered. The last block shows fit quality  $\chi^2/\text{DOF}$ .

Ensemble	$m_\rho$ (MeV)	$g_{\rho\pi\pi}$	$\Gamma_\rho$ (MeV)	$\chi^2/\text{DOF}$
(0.00155, 0.031)	791(10)	5.82(35)	128(16)	3.73/7
(0.0031, 0.0031)	827(8)	6.09(21)	104(7)	3.55/7
(0.0031, 0.031)	836(8)	6.03(28)	106(10)	9.09/7
(0.00465, 0.031)	875(9)	5.88(21)	76.4(5.7)	12.3/7
(0.0062, 0.031)	915(9)	5.80(17)	57.6(3.6)	12.5/5
(0.005, 0.005)	840(8)	5.90(19)	90.8(5.7)	2.16/7

<sup>5</sup> Other parametrizations have been recently discussed for the  $\rho$  resonance in Refs. [18, 52–54]. Additionally, the RQCD Collaboration found that all the resonant masses obtained from other parametrizations are in perfect agreement with those from Breit-Wigner [22].

<sup>6</sup> It is interesting and important to note that for the (0.0031, 0.031) and (0.0031, 0.0031) lattice ensembles, the pion masses are almost the same and  $L$  is identical; nonetheless, the strange sea quarks for two lattice ensembles are quite different. However, the discrepancies of the resonance mass  $m_\rho$  for two ensembles are clearly noticed, which indicates the influence of the strange sea quark.

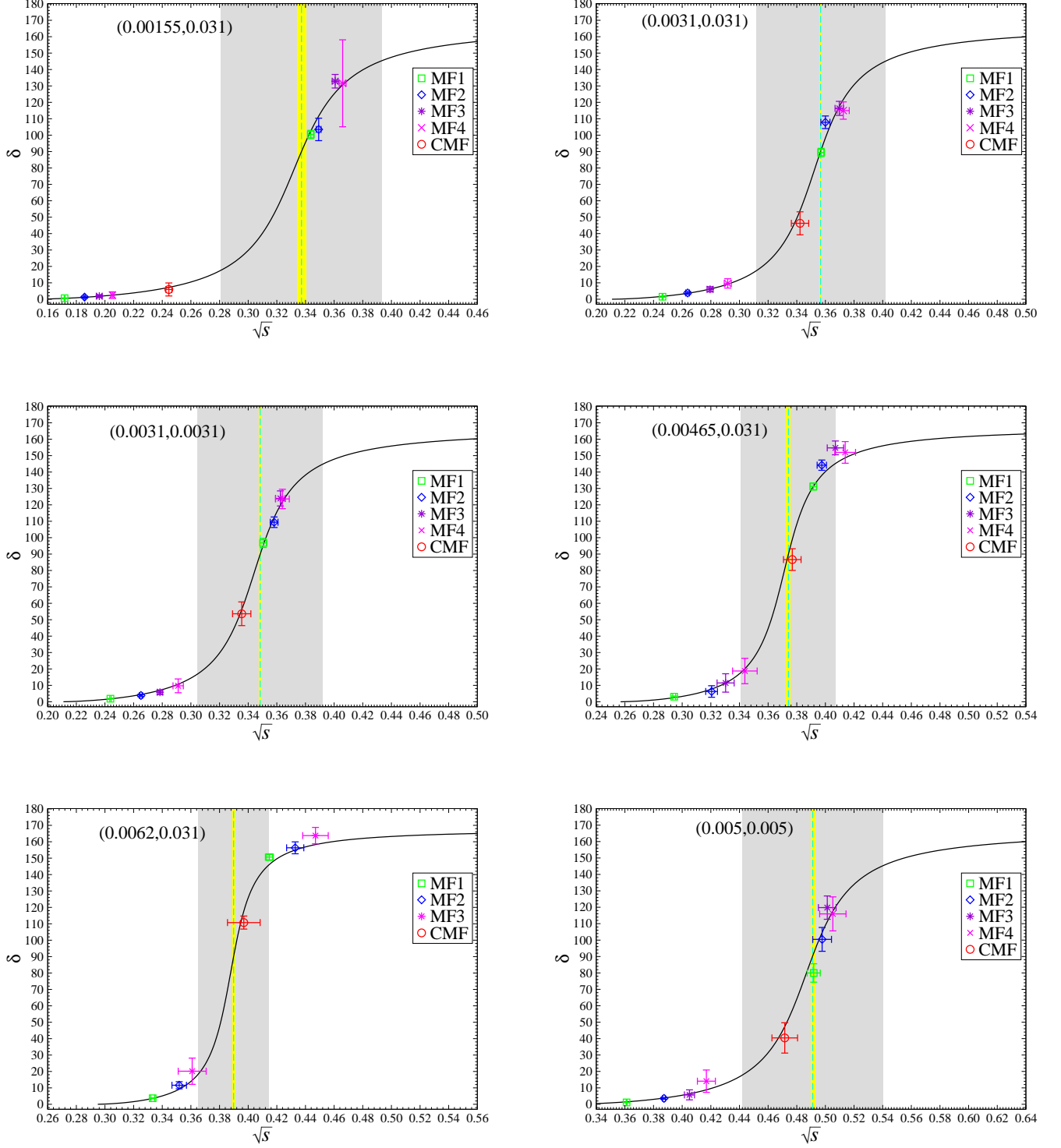


FIG. 6. Results of the scattering phase shifts and effective range formula fits for the ensembles (0.0031, 0.031) (upper left), (0.0031, 0.0031) (upper right), (0.00465, 0.031) (middle left), (0.0062, 0.031) (middle right), (0.005, 0.005) (bottom left), and (0.005, 0.05) (bottom right). The scattering phase shifts are calculated in the CMF, MF1, MF2, MF3 and MF4, respectively. The solid black curves exhibit the central values of the effective range formula fits. The dashed cyan lines display the resonance masses  $am_\rho$ , the narrow yellow bands display their uncertainties, and the resonance regions  $am_\rho \pm a\Gamma$  are shown in the shadowed grey boxes.

### C. Comparison with other results

In Fig. 7, we compare our lattice results of  $\rho$  resonance parameters from the MILC Asqtad-improved staggered fermions (2 + 1 or 3 flavors) with some other lattice studies: the improved Wilson fermions (2 flavors, CP-PACS [11]), the maximally twisted mass fermions (2 flavors, ETMC [13]), the tree-level improved clover-Wilson fermions (2 flavors, Lang *et al.* [15]), the nHYP-smearred clover fermions (2 flavors, Pelissier and Alexandru [17]), the nonperturbatively  $O(a)$ -improved Wilson fermion (2 flavors, PACS-CS [16]), the anisotropic Clover Wilson fermions (2 + 1 flavors, HSC [18, 19]), the improved Wilson fermions (2 + 1 flavors, Frison *et al.* [14]), the anisotropic Wilson clover fermions (2 + 1 flavors, Bulava *et al.* [20]), the nHYP-smearred clover fermions (2 flavors, Guo *et al.* [21]), and the nonperturbatively improved Wilson fermions (2 flavors, RQCD [22]). The top panel of Fig. 7 plots the effective coupling constant  $g_{\rho\pi\pi}$  and the bottom panel shows the resonance mass  $m_\rho$ . The systematic uncertainty for the determination of the lattice spacing is added to the statistical error in quadrature. It is important to note that our lattice results obtained with staggered fermions are reasonably consistent with those using other actions, which have quite different systematics.

The effective coupling constant  $g_{\rho\pi\pi}$  is dimensionless, and thus practically has a weak quark mass dependence. We also observe that the results of  $g_{\rho\pi\pi}$  from all the lattice studies are almost consistent in top panel of Fig. 7. Our results of  $g_{\rho\pi\pi}$  are well consistent with other lattice studies and were determined with the similar precision. Indeed, the stability of the results for  $g_{\rho\pi\pi}$  with respect to other magnitudes was anticipated in Ref. [55].

It is worth mentioning that the resonance mass  $m_\rho$  is very sensitive to the pion masses. In order to avoid the artificial systematic error from the determination of the lattice spacings, which are used to measure  $m_\rho$  and  $m_\pi$  in lattice units, it is proper to adopt dimensionless quantities to compare the resonance mass  $m_\rho$  with each other, and it is natural to use the Sommer scale  $r_0$  [56]. The bottom panel of Fig. 7 shows the resonance mass  $m_\rho$ , where  $m_\rho$  and  $m_\pi$  are both scaled with the Sommer scale  $r_0$  [56]. The lattice spacings  $a$  and  $r_0$  for six lattice ensembles used in the present work have been professionally determined by MILC in Refs. [29, 30, 37], we can directly quote these results;<sup>7</sup> Lang *et al.* determined the lattice spacing by inputting the  $r_0 = 0.48$  fm [15] and Pelissier and Alexandru fixed the lattice spacing by setting  $r_0 = 0.5$  fm [17]. The value of  $r_0$  for the ETMC gauge configuration was determined to be  $r_0/a = 5.32(5)$  [57], the PACS-CS gauge configuration has been reported as  $r_0/a = 5.427(51)$  [58] and that

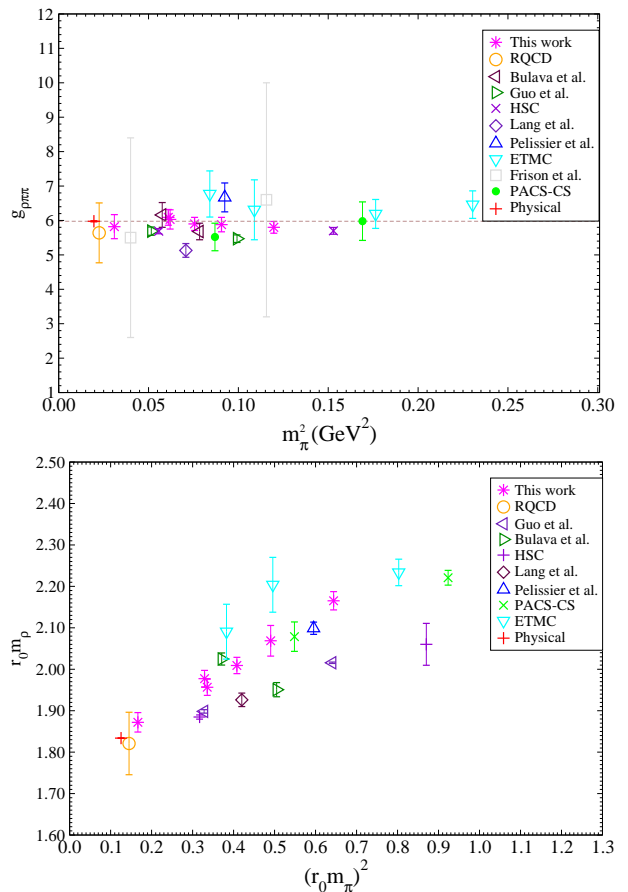


FIG. 7. Comparison of our results with other lattice studies. The top panel shows the effective coupling constant  $g_{\rho\pi\pi}$  as a function of  $m_\pi^2$ . The bottom panel shows the resonance mass  $m_\rho$ , where  $m_\rho$  and  $m_\pi$  are scaled with Sommer scale  $r_0$  [56]. The red pluses indicate the corresponding PDG values.

for HSC as  $r_0 = 0.454$  fm [59]. The RQCD determined the lattice spacing by setting  $r_0 = 0.501$  fm [22, 60], and Guo *et al.* usually set  $r_0 = 0.5$  fm [21]. We should remark at this point that the relevant PDG value in Fig. 7 is just scaled with MILC's determinations of  $r_0$  on the same lattices of this work [29, 30, 37] since it is reasonably compatible with Sommer's continuum extrapolation of  $r_0$  for the published  $N_f > 2$  determinations [61].

Nonetheless, from the bottom panel of Fig. 7, large differences for the resonance mass  $m_\rho$  are still discerned. Note that there has been no attempt so far with a continuum limit extrapolation. As pointed out in Ref. [16], there exist some other possible issues to interpret this discrepancy, such as the discretization error, the influence of the strange sea quark (as we already discern in Sec. V B), the issue of the isospin breaking and the reliability of the effective range parametrization, ad son forth. In any case, the robust extraction of the resonance mass  $m_\rho$  definitely need more lattice simulations in the vicinity of the physical point, as well as a continuum limit extrapolation.

<sup>7</sup> This work benefits a lot from the MILC Collaboration; without their published data, we could not launch this work.

### D. Quark mass dependence

So far, only the ETMC Collaboration has discussed the quark mass dependence of  $\rho$  resonance parameters [13] the other lattice works have been studied with one pion mass or two pion masses [11–22]. Since, six quark masses are used in the present study, we are now in a position to examine the pion mass dependence of the  $\rho$  resonance parameters.

The quark mass dependence of the  $\rho$  resonance parameters are discussed with effective field theory in Ref. [62]. The pion mass dependence of the  $\rho$  resonance mass  $m$  and  $\rho$  decay width  $\Gamma_\rho$  can be generally expressed as [62]

$$m_\rho = m_\rho^0 + C_{m1}M_\pi^2 + C_{m2}m_\pi^3 + O(m_\pi^4), \quad (30)$$

$$\Gamma_\rho = \Gamma_\rho^0 + C_{\Gamma1}m_\pi^2 + C_{\Gamma2}m_\pi^3 + O(m_\pi^4). \quad (31)$$

In the top panel of Fig. 8, we display the  $\rho$  resonance mass as a function of  $m_\pi^2$ , together with a fit to Eq. (30); these are also summarized on the left side of Table VI. After the chiral extrapolation to the physical point, we obtain the physical  $\rho$  resonance mass  $m_{\rho;\text{phys}} = 780(16)$  MeV, where the uncertainty is solely estimated by the fitted statistical errors of the three coefficients in Eq. (30) that are listed in the left side of Table VI. It is obvious that our physical  $\rho$  resonance mass  $m_{\rho;\text{phys}}$  is in good agreement with the PDG value of the  $\rho$ -meson mass  $m_{\rho;\text{PDG}} = 775.26(25)$  MeV [1] within the statistical errors, which is indicated by the red plus point in the top panel of Fig. 8.

As explained in Ref. [13], since the ETMC Collaboration carried out the lattice calculations at the relatively large pion masses (from 290 to 480 MeV), their obtained physical  $\rho$  resonance mass  $m_{\rho;\text{phys}}$  is relatively high compared to the PDG value even using the  $O(q^4)$  extrapolations. On the other hand, this work carries out a study with the relatively small pion mass (from 176 to 346 MeV), and with the more lattice ensembles. Note that the RQCD Collaboration recently worked at nearly physical quark masses [22].

TABLE VI. Summary of the  $\rho$  resonance mass  $m_\rho$  and  $\rho$  decay width  $\Gamma_\rho$  fitting with Eqs. (30) and (31), respectively. The values of  $m_\rho^0$  and  $\Gamma_\rho^0$  are given in units of GeV, those of  $C_{m1}$  and  $C_{\Gamma1}$  are given in units of  $\text{GeV}^{-1}$ , and those of  $C_{m2}$  and  $C_{\Gamma2}$  are given in units of  $\text{GeV}^{-2}$ . The corresponding fits result in fit qualities  $\chi^2/\text{DOF}=2.06/3$ ,  $0.33/3$ , respectively.

Fit of $m_\rho$ to	Eq. (30)	Fit of $\Gamma_\rho$ to	Eq. (31)
$m_\rho^0$	0.768(14)	$\Gamma_\rho^0$	0.166(15)
$C_{m1}$	0.38(42)	$C_{\Gamma1}$	-1.33(44)
$C_{m2}$	2.49(96)	$C_{\Gamma2}$	1.21(96)

<sup>8</sup> Note that  $m_\rho$  and  $\Gamma_\rho$  are statistically correlated, indicating that the coefficients  $C_{m_i}$  and  $C_{\Gamma_i}$  ( $i = 1, 2$ ) are not independent from each other. Therefore, following the strategy of Refs. [63], Xu *et al* introduced the complex pole parameter  $Z$  to fit their data [13].

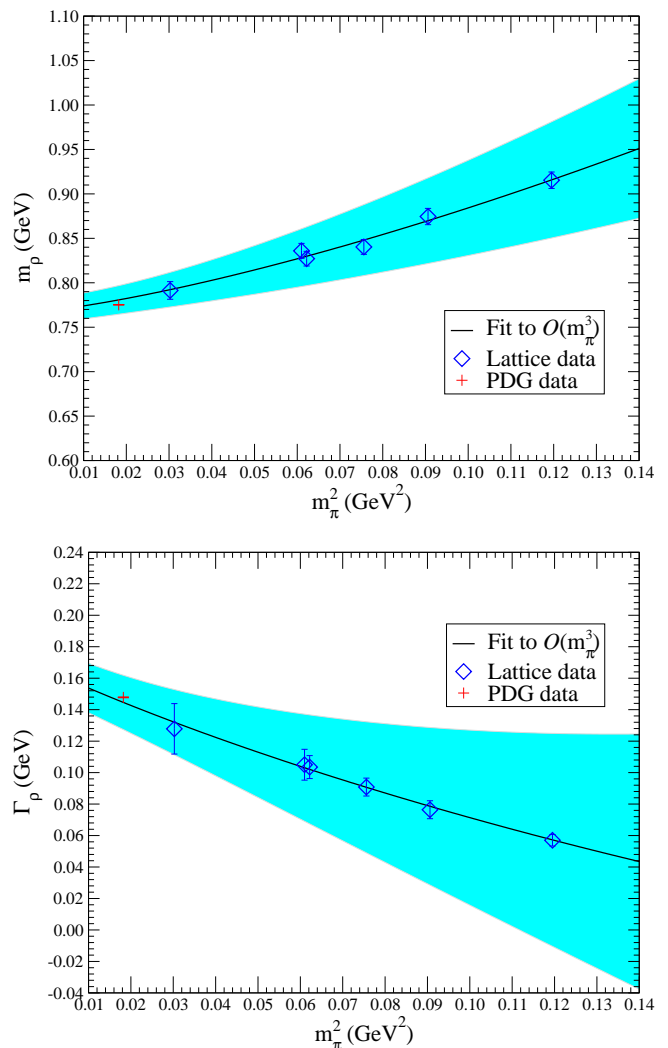


FIG. 8. The lattice-measured  $\rho$  resonance parameters as the functions of the pion mass squared. The upper panel exhibits the  $\rho$ -meson resonance mass and the lower panel shows the  $\rho$ -meson decay width. The cyan bands correspond to the fits to our six data points using the Eq. (30) and Eq. (31), respectively, and the solid black curves are the central values of the corresponding fits. The red plus points indicate the relevant PDG values.

In practice, the decay width  $\Gamma_\rho$  can be estimated through Eq. (29), where the statistical errors are estimated from the statistical errors of both  $g_{\rho\pi\pi}$  and  $m_\rho$ . Therefore, our lattice-extracted decay widths  $\Gamma_\rho$  definitely indicate a union of the two factors. In the bottom panel of Fig. 8, we exhibit the decay width  $\Gamma_\rho$  as a function of the pion mass squared, along with a fit to Eq. (31); these are also summarized in the right side of Table VI. Since Eq. (29) naturally regresses to  $\Gamma_\rho = g_\rho g_{\rho\pi\pi}^2 / (48\pi)$  in the chiral limit, it often leads to a good value of  $\Gamma_\rho$  with the better value of  $m_\rho$ . Moreover, the error of  $g_{\rho\pi\pi}$  will be more quickly propagated in the  $\Gamma_\rho$  than that of  $m_\rho$ . After the chiral extrapolation to the physical point, our physical  $\rho$  decay width  $\Gamma_{\rho;\text{phys}} = 144.6(17.3)$  MeV,



where the uncertainty is solely estimated by the fitted statistical errors of the three coefficients in Eq. (31) that are listed in the right side of Table VI. Our physical  $\rho$  decay width  $\Gamma_{\rho;\text{phys}}$ , is slightly lower than the PDG value  $\Gamma_{\rho;\text{PDG}} = 147.8(0.9)$  MeV [1], but it is in reasonable agreement with the PDG value within the statistical errors, which is indicated by the red plus point in the bottom panel of Fig. 8. Nonetheless, it is worth mentioning that our lattice-measured  $\rho$  resonance parameters are obviously much less accurate than the PDG values [1].

## VI. CONCLUSIONS AND OUTLOOK

In this work, we for the first time employ the  $N_f = 2+1$  or 3 flavors of the MILC Asqtad-improved staggered fermions at pion masses ranging from 176 to 346 MeV to carry out the lattice computation of the  $p$ -wave  $I = 1$   $\pi\pi$  scattering phase shifts near the  $\rho$  resonance region. At all the pion masses, the physical kinematics for the  $\rho$ -meson decay,  $m_\pi/m_\rho < 0.5$ , is satisfied. Additionally, from Table II, we note that our lattice volumes all have  $m_\pi L > 4$ ; thus, finite-size effects are negligible, and the Lüscher formulas are perfectly satisfied, since the finite-size effects are exponentially suppressed with the combination  $m_\pi L$ . In particular, we marked out the resonance region by simultaneously adopting five Lorentz frames (CMF, MF1, MF2, MF3, and MF4).

Moreover, we for the first time investigated  $\rho$  resonance parameters with the moving-wall source technique [23, 24], a nonstochastic source method. We have shown that the lattice computation of the  $p$ -wave scattering phase for the  $I = 1$   $\pi\pi$  system using the moving-wall source and then the estimation of the decay width of the  $\rho$  meson are feasible and effective, and can be comparable with the stochastic source method [11–14, 16–19, 22], or its variants (the distillation method, etc. [15, 20, 21]). Most of all, we extracted the  $\rho$ -meson decay width from the scattering phase data and demonstrated that it is reasonably comparable with the  $\rho$ -meson decay width from PDG within the statistical errors.

We evaluated the scattering phase from the seven or nine energy levels for the six lattice ensembles by the Lüscher finite-size methods. The scattering phases are fitted with the effective range formula to extract the  $\rho$  resonance mass  $m_\rho$ , the decay width  $\Gamma_\rho$  and the effective coupling  $g_{\rho\pi\pi}$ . Despite not considering the inherent relation between  $m_\rho$  and  $\Gamma_\rho$ , we conducted a fit guided by the effective field theory to our results at six pion masses. This provided an alternative means of the chiral extrapolation to the physical point.

After the chiral extrapolation to the physical point, we obtain the physical  $\rho$ -meson mass  $m_{\rho;\text{phys}} = 780(16)$  MeV, which is in agreement with the experimental value  $m_{\rho;\text{PDG}} = 775.26(25)$  MeV [1], and the decay width  $\Gamma_{\rho;\text{phys}} = 144.6(17.3)$  MeV, which is slightly low relative to the experimental value  $\Gamma_{\rho;\text{PDG}} = 147.8(0.9)$  MeV [1]. Moreover, our results are compatible with most recent

lattice studies [11–22]. It is obvious that our lattice computations cannot yet match the experimental accuracy.

With the development of better algorithms, more efficient codes, and an increase in computational resources, the lattice calculations of the  $\rho$  resonance parameters with large  $L$ , small pion, and fine lattice will become possible, which will make the lattice simulation more accurate [22] (see the Appendix for more details). With this aim in mind, our ongoing lattice studies will be carried out with the MILC superfine gauge configuration ( $a \approx 0.6$  fm,  $L = 48$ , and beyond), and even with the MILC ultrafine gauge configuration ( $a \approx 0.45$  fm and  $L = 64$ ). These studies will include several lattice spacings, which enables us to make a continuum limit extrapolation. Furthermore, working close to the physical pion mass with large  $L$  or very fine lattice are crucial for lattice investigations of the scattering processes involving thresholds, e.g.,  $X(3872)$ ,  $D\bar{D}^*$ , and beyond [64].

## ACKNOWLEDGMENTS

This work is partially supported by both the National Magnetic Confinement Fusion Program of China (Grant No. 2013GB109000) and the Fundamental Research Funds for the Central Universities (Grant No. 2010SCU23002). We would like to express our deep appreciation to the MILC Collaboration for allowing us to use the MILC gauge configurations and MILC codes. We would like to thank the NERSC for providing a convenient platform to download the MILC gauge configurations. We sincerely thank Carleton DeTar for his introduction to Karl Jansen’s lattice works about six years ago and indoctrinating me in the necessary theoretical knowledge and computational skills for this work. We especially thank Eulogio Oset for his enlightening and constructive comments and corrections. The author must express my respect to Geng Liseng, Liu Chuan, and Chen ying for reading this manuscript and give some useful comments. Once again, we cordially express our boundless gratitude to prof. Hou qing’s strong support, prof. He Yan’s contributing to us two powerful workstations, and prof. Fujun Gou’s vigorous supports, otherwise, it is impossible for us to conduct this expensive work, and have an opportunity to fulfill it. We should show our appreciations to profs. He Yan, Huang Ling, Wang Jun, An Zhu, Liu Ning and Fu Zhe, etc. for donating us enough removable hard drives to store the quark propagators for this work. We also express gratitude to the Institute of Nuclear Science and Technology, Sichuan University, and Chengdu Jiaxiang Foreign Language School, from which the computer resources and electricity costs for this study were furnished. Numerical calculations for this work were carried out at both PowerLeader Clusters and AMAX, CENTOS, HP, ThinkServer workstations.

### Appendix A: The noise-to-signal ratio of the correlator

In Ref. [24], the noise-to-signal ratio of the two-point function at zero momentum evaluated with  $N_{cfg}$  independent gauge configurations is estimated as

$$R_{SN}^2 \propto \sqrt{\frac{1}{N_{cfg}L^3}} \exp[(m_M - m_\pi)t] \quad (\text{A1})$$

where  $L$  is the lattice spatial dimension, and  $m_M$  is the desired meson mass. The superscript in  $R$  indicates that this is the *two*-point function.

It is straightforward to extend this expression to the two-point function at nonzero momentum  $\mathbf{p}$

$$R_{SN}^2 \propto \sqrt{\frac{1}{N_{cfg}L^3}} \exp[(E_M - m_\pi)t] \quad (\text{A2})$$

where the meson energy  $E_M = \sqrt{m_M^2 + \mathbf{p}^2}$ ,  $\mathbf{p} = \frac{2\pi}{L}\mathbf{n}$ . In fact, this expression can be inferred from the analytical arguments in Refs. [27, 28]. In practice, in order to improve the statistics, the correlators are calculated from a given number of time slices ( $N_{\text{slice}}$ ). The corresponding noise-to-signal ratio can be roughly evaluated as

$$R_{SN}^2 \propto \sqrt{\frac{1}{N_{cfg}N_{\text{slice}}L^3}} \exp[(E_M - m_\pi)t]. \quad (\text{A3})$$

Here we crudely assume that the calculations from different time slices are independent. In our concrete numerical calculations [65], we indeed adjust the values of  $N_{\text{slice}}$  to obtain the relevant masses with the desired precision; at the same time, we found  $R_{SN}^2 \propto 1/(N_{cfg})^\alpha$ , where the

exponent  $\alpha = 0.4 \sim 0.5$ . Therefore, the relationship of the noise-to-signal ratio with  $N_{\text{slice}}$  in Eq. (A3) is approximately satisfied.

The dramatic deterioration of the signal as the momentum increases is shown in Fig. 2 of Ref. [27]. This quite impressive result indicates that the expected asymptotic behavior given in Eq. (A3) is generally met. We should remark at this point that, in practice, the asymptotic trend given in Eq. (A3) can effectively guide us how to improve the relevant statistical errors.

For the  $\pi\pi$  scattering (two pions with the momentum  $\mathbf{p}$  and  $\mathbf{q}$ , respectively), the noise-to-signal ratio of the four-point function can be straightforwardly generalized as [24]

$$R_{SN}^4 \propto \sqrt{\frac{1}{N_{cfg}N_{\text{slice}}L^3}} \exp[(E_\pi(\mathbf{p}) + E_\pi(\mathbf{q}) - 2m_\pi)t], \quad (\text{A4})$$

where the energy  $E_\pi(\mathbf{p} = \frac{2\pi}{L}\mathbf{n}) = \sqrt{m_\pi^2 + \frac{4\pi^2}{L^2}\mathbf{n}^2}$  and  $E_\pi(\mathbf{q} = \frac{2\pi}{L}\mathbf{m}) = \sqrt{m_\pi^2 + \frac{4\pi^2}{L^2}\mathbf{m}^2}$ .

According to the above analytical discussions, we can readily deduce that the most efficient way to improve the relevant noise-to-signal ratios is to use very fine gauge configurations where the temporal lattice spacing  $a_t$  and the spatial lattice spacing  $a_s$  are pretty small ( $a_s = a_t$ ), since the energy and the mass are measured in lattice  $a_t$  units  $a_tm$  and  $a_tE$ ; and equivalently, the use of the anisotropic gauge configurations, where  $a_t$  is much smaller than  $a_s$ , is also a powerful approach to improve the relevant noise-to-signal ratios [18, 19]. In addition, if we use the lattice ensembles with larger lattice spatial dimensions  $L$ , and sum the correlators over all the time slices (i.e.,  $N_{\text{slice}} = T$ , where  $T$  is the lattice temporal dimension), the signals of the correlators should also be significantly improved.

- 
- [1] K. A. Olive *et al.* (Particle Data Group), Review of Particle Physics (RPP), Chin. Phys. C **38**, 090001 (2014).
  - [2] S. A. Gottlieb, P. B. MacKenzie, H. B. Thacker and D. Weingarten, Hadronic couplings constants in lattice gauge theory, Nucl. Phys. B **263**, 704 (1986); S. A. Gottlieb, P. B. Mackenzie, H. B. Thacker and D. Weingarten, The  $\rho - \pi\pi$  coupling constant in lattice gauge theory, Phys. Lett. B **134**, 346 (1984).
  - [3] N. Vasanti, Some calculations in lattice gauge theory, Nucl. Phys. B **118**, 533 (1977).
  - [4] R. D. Loft and T. A. DeGrand, Vector meson decay into pseudoscalars from quenched lattice QCD, Phys. Rev. D **39**, 2692 (1989).
  - [5] R. L. Altmeyer, M. Gockeler, R. Horsley, E. Laermann, G. Schierholz and P. M. Zerwas, Hadronic coupling constants in lattice QCD, Z. Phys. C **68**, 443 (1995).
  - [6] C. McNeile *et al.* (UKQCD Collaboration), Hadronic decay of a vector meson from the lattice, Phys. Lett. B **556**, 177 (2003).
  - [7] K. Jansen, C. McNeile, C. Michael, and C. Urbach (ETM Collaboration), Meson masses and decay constants from unquenched lattice QCD, Phys. Rev. D **80**, 054510 (2009).
  - [8] M. Lüscher, Two particle states on a torus and their relation to the scattering matrix, Nucl. Phys. B **354**, 531 (1991).
  - [9] M. Lüscher, U. Wolff, How to calculate the elastic scattering matrix in two-dimensional quantum field theories by numerical simulation, Nucl. Phys. B **339**, 222 (1990).
  - [10] K. Rummukainen and S. A. Gottlieb, Resonance scattering phase shifts on a nonrest frame lattice, Nucl. Phys. B **450**, 397 (1995); C. H. Kim, C. T. Sachrajda, and S. R. Sharpe, Finite-volume effects for two-hadron states in moving frames, Nucl. Phys. B **727**, 218 (2005); N. H. Christ, C. Kim and T. Yamazaki, Finite volume corrections to the two-particle decay of states with nonzero momentum, Phys. Rev. D **72**, 114506 (2005); M. Doring, U. G. Meissner, E. Oset and A. Rusetsky,

- Scalar mesons moving in a finite volume and the role of partial wave mixing, *Eur. Phys. J. A* **48**, 114 (2012).
- [11] S. Aoki, M. Fukugita, K.-I. Ishikawa, N. Ishizuka, K. Kanaya, Y. Kuramashi, Y. Namekawa, M. Okawa, K. Sasaki, A. Ukawa, and T. Yoshié, Lattice QCD calculation of the rho Meson Decay Width, *Phys. Rev. D* **76**, 094506 (2007).
- [12] M. Gockeler *et al.* (QCDSF Collaboration), Extracting the rho resonance from lattice QCD simulations at small quark masses, *PoS LATTICE 2008*, 136 (2008).
- [13] X. Feng, K. Jansen and D. B. Renner, Resonance parameters of the rho-meson from lattice QCD, *Phys. Rev. D* **83**, 094505 (2011).
- [14] J. Frison *et al.* (Budapest-Marseille-Wuppertal Collaboration), Rho decay width from the lattice, *Proc. Sci. LATTICE 2010* (2010) 139.
- [15] C. B. Lang, D. Mohler, S. Prelovsek and M. Vidmar, Coupled channel analysis of the rho meson decay in lattice QCD, *Phys. Rev. D* **84**, 054503 (2011).
- [16] S. Aoki, K.-I. Ishikawa, N. Ishizuka, K. Kanaya, Y. Kuramashi, Y. Namekawa, M. Okawa, Y. Taniguchi, A. Ukawa, N. Ukita, T. Yamazaki, and T. Yoshié,  $\rho$  Meson decay in 2+1 flavor lattice QCD, *Phys. Rev. D* **84**, 094505 (2011).
- [17] C. Pelissier and A. Alexandru, Resonance parameters of the rho-meson from asymmetrical lattices, *Phys. Rev. D* **87**, 014503 (2013).
- [18] J. J. Dudek, R. G. Edwards and C. E. Thomas, Energy dependence of the  $\rho$  resonance in  $\pi\pi$  elastic scattering from lattice QCD, *Phys. Rev. D* **87**, 034505 (2013).
- [19] D. J. Wilson, R. A. Briceño, J. J. Dudek, R. G. Edwards and C. E. Thomas, Coupled  $\pi\pi, K\bar{K}$  scattering in  $P$ -wave and the  $\rho$  resonance from lattice QCD, *Phys. Rev. D* **92**, 094502 (2015).
- [20] J. Bulava, B. Hörz, B. Fahy, K. J. Juge, C. Morningstar, and C. H. Wong, Pion-pion scattering and the timelike pion form factor from  $N_f = 2 + 1$  lattice QCD simulations using the stochastic LapH method, *Proc. Sci., LATTICE2015* (2016) 069 [arXiv:1511.02351].
- [21] D. Guo, A. Alexandru, R. Molina and M. Doering, Rho resonance parameters from lattice QCD, *Phys. Rev. D* **94**, 034501 (2016).
- [22] G. S. Bali, S. Collins, A. Cox, G. Donald, M. Göckeler, C. B. Lang, and A. Schäfer,  $\rho$  and  $K^*$  resonances on the lattice at nearly physical quark masses and  $N_f = 2$ , *Phys. Rev. D* **93**, 054509 (2016).
- [23] Y. Kuramashi, M. Fukugita, H. Mino, M. Okawa and A. Ukawa, Lattice QCD calculation of full pion scattering lengths, *Phys. Rev. Lett.* **71**, 2387 (1993).
- [24] M. Fukugita, Y. Kuramashi, M. Okawa, H. Mino, and A. Ukawa, Hadron scattering lengths in lattice QCD, *Phys. Rev. D* **52**, 3003 (1995).
- [25] Z. Fu, Preliminary lattice study of  $\sigma$  meson decay width, *J. High Energy Phys.* **07** (2012) 142. Z. Fu, Preliminary lattice study of  $\kappa$  meson decay width, *J. High Energy Phys.* **01** (2012) 017; Z. Fu and K. Fu, Lattice QCD study of the  $K^*(892)$  meson decay width, *Phys. Rev. D* **86**, 094507 (2012); Z. Fu, Rummukainen-Gottlieb formula on two-particle system with different mass, *Phys. Rev. D* **85**, 014506 (2012).
- [26] Z. Fu, Lattice QCD calculation of  $\pi\pi$  scattering length, *Commun. Theor. Phys.* **57**, 78 (2012); Z. Fu, Lattice QCD study of the s-wave  $\pi\pi$  scattering lengths in the  $I=0$  and 2 channels, *Phys. Rev. D* **87**, 074501 (2013); Z. Fu, Lattice study on  $\pi K$  scattering with moving wall source, *Phys. Rev. D* **85**, 074501 (2012); Z. Fu, Preliminary study of the  $I=1$   $K\bar{K}$  scattering length from lattice QCD, *Eur. Phys. J. C* **72**, 2159 (2012).
- [27] M. Della Morte, B. Jaeger, T. Rae, and H. Wittig, Improved interpolating fields for hadrons at nonzero momentum, *Eur. Phys. J. A* **48**, 139 (2012).
- [28] G. Parisi, The strategy for computing the hadronic mass spectrum, *Phys. Rept.* **103**, 203 (1984); G. P. Lepage, The analysis of algorithms for lattice field theory, Report No. CLNS-89-971.
- [29] C. Bernard, C. DeTar, M. Di Pierro, A. X. El-Khadra, R. T. Evans *et al.* (Fermilab Lattice and MILC Collaborations), Tuning fermilab heavy quarks in 2+1 flavor lattice QCD with application to hyperfine splittings, *Phys. Rev. D* **83**, 034503 (2011).
- [30] A. Bazavov *et al.* (MILC Collaboration), Nonperturbative QCD simulations with 2+1 flavors of improved staggered quarks, *Rev. Mod. Phys.* **82**, 1349 (2010).
- [31] T. Yamazaki, S. Aoki, M. Fukugita, K.-I. Ishikawa, N. Ishizuka, Y. Iwasaki, K. Kanaya, T. Kaneko, Y. Kuramashi, M. Okawa, A. Ukawa, and T. Yoshié (CP-PACS Collaboration),  $I = 2$   $\pi\pi$  scattering phase shift with two flavors of O(a) improved dynamical quarks, *Phys. Rev. D* **70**, 074513 (2004).
- [32] M. Doring, U. -G. Meissner, E. Oset, and A. Rusetsky, Unitarized chiral perturbation theory in a finite volume: Scalar meson sector, *Eur. Phys. J. A* **47**, 139 (2011).
- [33] M. Gockeler, R. Horsley, M. Lage, U. G. Meissner, P. E. L. Rakow, A. Rusetsky, G. Schierholz, and J. M. Zanotti, Scattering phases for meson and baryon resonances on general moving-frame lattices, *Phys. Rev. D* **86**, 094513 (2012).
- [34] B. Blossier, M. Della Morte, G. von Hippel, T. Mendes and R. Sommer, On the generalized eigenvalue method for energies and matrix elements in lattice field theory, *J. High Energy Phys.* **04** (2009) 094.
- [35] C. DeTar and S. H. Lee, Variational method with staggered fermions, *Phys. Rev. D* **91**, 034504 (2015).
- [36] C.W. Bernard, T. Burch, K. Orginos, D. Toussaint, T. DeGrand, C. DeTar, S. Datta, S. Gottlieb, U. Heller, and R. Sugar, The QCD spectrum with three quark flavors, *Phys. Rev. D* **64**, 054506 (2001).
- [37] C. Aubin, C. Bernard, C. DeTar, J. Osborn, S. Gottlieb, E. B. Gregory, D. Toussaint, U. M. Heller, J. E. Hetrick, and R. Sugar, Light hadrons with improved staggered quarks: Approaching the continuum limit, *Phys. Rev. D* **70**, 094505 (2004).
- [38] S. R. Sharpe, R. Gupta and G. W. Kilcup, Lattice calculation of  $I = 2$  pion scattering length, *Nucl. Phys. B* **383**, 309 (1992).
- [39] S. Dürr, C. Hoelbling, and U. Wenger, Staggered eigenvalue mimicry, *Phys. Rev. D* **70**, 094502 (2004); C. Bernard, Staggered chiral perturbation theory and the fourth-root trick, *Phys. Rev. D* **73**, 114503 (2006); C. Bernard, M. Golterman, Y. Shamir, and S. R. Sharpe, Comment on: “Chiral anomalies and rooted staggered fermions”, *Phys. Lett. B* **649**, 235 (2007); C. Bernard, M. Golterman, and Y. Shamir, Observations on staggered fermions at nonzero lattice spacing, *Phys. Rev. D* **73**, 114511 (2006); M. Creutz, Reply to: “Comment on: “Chiral anomalies and rooted staggered fermions””, *Phys. Lett. B* **649**, 241 (2007); A. Hasenfratz and R. Hoffmann, Validity of the rooted staggered determinant in

- the continuum limit, Phys. Rev. D **74**, 014511 (2006).
- [40] C. Aubin, C. Bernard, C. DeTar, J. Osborn, S. Gottlieb, E. B. Gregory, D. Toussaint, U. M. Heller, J. E. Hetrick, and R. Sugar (MILC Collaboration), Light pseudoscalar decay constants, quark masses, and low energy constants from three-flavor lattice QCD, Phys. Rev. D **70**, 114501 (2004).
- [41] M. F. L. Golterman, Staggered mesons, Nucl. Phys. B **273**, 663 (1986).
- [42] I. T. Drummond, S. Duane and R. R. Horgan, The stochastic method for numerical simulations: Higher order corrections, Nucl. Phys. B **220**, 119 (1983); S.-J. Dong and K.-F. Liu, Stochastic estimation with Z(2) noise, Phys. Lett. B **328**, 130 (1994); M. Foster and C. Michael (UKQCD Collaboration), Quark mass dependence of hadron masses from lattice QCD, Phys. Rev. D **59**, 074503 (1999).
- [43] D. Barkai, K. J. M. Moriarty and C. Rebbi, Hadron masses in quenched quantum chromodynamics, Phys. Lett. B **156**, 385 (1985); A. Mihaly, H. R. Fiebig, H. Markum and K. Rabitsch, Interactions between heavy-light mesons in lattice QCD, Phys. Rev. D **55**, 3077 (1997).
- [44] R. Gupta, A. Patel, and S. R. Sharpe,  $I = 2$  pion scattering amplitude with Wilson fermions, Phys. Rev. D **48**, 388 (1993).
- [45] X. Feng, K. Jansen and D. B. Renner, The  $\pi^+\pi^+$  scattering length from maximally twisted mass lattice QCD, Phys. Lett. B **684**, 268 (2010).
- [46] T. Umeda, Constant contribution in meson correlators at finite temperature, Phys. Rev. D **75**, 094502 (2007).
- [47] J. J. Dudek, R. G. Edwards and C. E. Thomas, S- and D-wave phase shifts in isospin-2  $\pi\pi$  scattering from lattice QCD, Phys. Rev. D **86**, 034031 (2012).
- [48] D. B. Kaplan, A method for simulating chiral fermions on the lattice, Phys. Lett. B **288**, 342 (1992); Y. Shamir, Chiral fermions from lattice boundaries, Nucl. Phys. B **406**, 90 (1993).
- [49] C. Bernard *et al.*, Status of the MILC light pseudoscalar meson project, Proc. Sci., LAT2007 (2007) 090.
- [50] C. B. Lang, L. Leskovec, D. Mohler, and S. Prelovsek,  $K\pi$  scattering for isospin 1/2 and 3/2 in lattice QCD, Phys. Rev. D **86**, 054508 (2012).
- [51] R. R. Akhmetshin *et al.* (CMD-2 Collaboration), Cross-section of the reaction  $e^+e^- \rightarrow \pi^+\pi^-\pi^+\pi^-$  below 1 GeV at CMD-2, Phys. Lett. B **475**, 190 (2000).
- [52] F. Von Hippel and C. Quigg, Centrifugal-barrier effects in resonance partial decay widths, shapes, and production amplitudes, Phys. Rev. D **5**, 624 (1972).
- [53] Z. Li, M. Guidry, T. Barnes and E. S. Swanson,  $I = 0, 1\pi\pi$  and  $I = 1/2K\pi$  scattering using quark Born diagrams, arXiv:hep-ph/9401326.
- [54] J. R. Pelaez and F. J. Yndurain, The pion-pion scattering amplitude, Phys. Rev. D **71**, 074016 (2005).
- [55] H. X. Chen and E. Oset,  $\pi\pi$  interaction in the  $\rho$  channel in finite volume, Phys. Rev. D **87**, 016014 (2013).
- [56] R. Sommer, A new way to set the energy scale in lattice gauge theories and its applications to the static force and  $\sigma_s$  in SU(2) Yang-Mills theory, Nucl. Phys. B **411**, 839 (1994).
- [57] R. Baron *et al.* (ETM Collaboration), Light meson physics from maximally twisted mass lattice QCD, JHEP **1008**, 097 (2010).
- [58] S. Aoki, K.-I. Ishikawa, N. Ishizuka, T. Izubuchi, D. Kadoh, K. Kanaya, Y. Kuramashi, Y. Namekawa, M. Okawa, Y. Taniguchi, A. Ukawa, N. Ukita, and T. Yoshié, 2+1 Flavor lattice QCD toward the physical point, Phys. Rev. D **79**, 034503 (2009).
- [59] H.W. Lin, S. D. Cohen, J. Dudek, R. G. Edwards, B. Joo, *et al.* (Hadron Spectrum Collaboration), First results from 2+1 dynamical quark flavors on an anisotropic lattice: Light-hadron spectroscopy and setting the strange-quark mass, Phys. Rev. D **79**, 034502 (2009).
- [60] G. S. Bali *et al.*, Nucleon mass and sigma term from lattice QCD with two light fermion flavors, Nucl. Phys. B **866**, 1 (2013).
- [61] R. Sommer, Scale setting in lattice QCD, Proc. Sci., LATTICE2013 (2014) 015.
- [62] E. E. Jenkins, A. V. Manohar and M. B. Wise, Chiral perturbation theory for vector mesons, Phys. Rev. Lett. **75**, 2272 (1995); J. Bijnens, P. Gosdzinsky, and P. Talavera, Vector meson masses in chiral perturbation theory, Nucl. Phys. B **501**, 495 (1997); D. B. Leinweber, A. W. Thomas, K. Tsushima and S. V. Wright, Chiral behavior of the rho meson in lattice QCD, Phys. Rev. D **64**, 094502 (2001); P. C. Bruns and U. G. Meissner, Infrared regularization for spin-1 fields, Eur. Phys. J. C **40**, 97 (2005); C. Hanhart, J. R. Pelaez and G. Rios, Quark mass dependence of the rho and sigma from dispersion relations and Chiral Perturbation Theory, Phys. Rev. Lett. **100**, 152001 (2008).
- [63] D. Djukanovic, J. Gegelia, A. Keller, and S. Scherer, Complex-mass renormalization in chiral effective field theory, Phys. Lett. B **680**, 235 (2009).
- [64] C. B. Lang, L. Leskovec, D. Mohler, S. Prelovsek and R. M. Woloshyn,  $D_s$  mesons with  $DK$  and  $D^*K$  scattering near threshold, Phys. Rev. D **90**, 034510 (2014).
- [65] Z. Fu,  $I=1/2$  low-lying mesons in lattice QCD, Chin. Phys. C **39**, 083101 (2015).